Supporting Information for

The role of ionic liquid breakdown in the electrochemical metallization of VO_2: An NMR study of gating mechanisms and VO_2 reduction

Michael A. Hope,[1] Kent J. Griffith,[1] Bin Cui,[2] Fang Gao,[2] Siân E. Dutton,[3] Stuart S. P. Parkin,[2] Clare P. Grey[1,*]

[1] *Department of Chemistry, University of Cambridge, Lensfield Road, Cambridge CB2 1EW, UK.*
[2] *Max Planck Institute of Microstructure Physics, Halle (Saale) D06120, Germany.*
[3] *Cavendish Laboratory, JJ Thomson Avenue, Cambridge CB3 0HE, UK.*

Contents

1 Calibration of the Ag Wire Pseudo-Reference Electrode

To calibrate the Ag wire pseudo-reference electrode, cyclic voltammograms (CVs) were recorded of 10 mM ferrocene (Fc) dissolved in the EMIm TFSI ionic liquid electrolyte, at room temperature and in steps of 25 °C between 50 °C and 175 °C, inclusive (Figure 1a). The potential of the pseudo-reference electrode relative to the ferrocene/ferrocenium (Fc/Fc^+) redox couple can then be found at each temperature from the (negative of the) average of the anodic and cathodic peak potentials in the CVs (Figure 1b). The potential of the Ag wire pseudo-reference electrode increases with increasing temperature due to greater solubility of Ag^+ in the ionic liquid. The ferrocene/ferrocenium couple cannot be measured at 200 °C as ferrocene decomposes at this temperature,[1] so the potential of the reference electrode was extrapolated to this temperature.

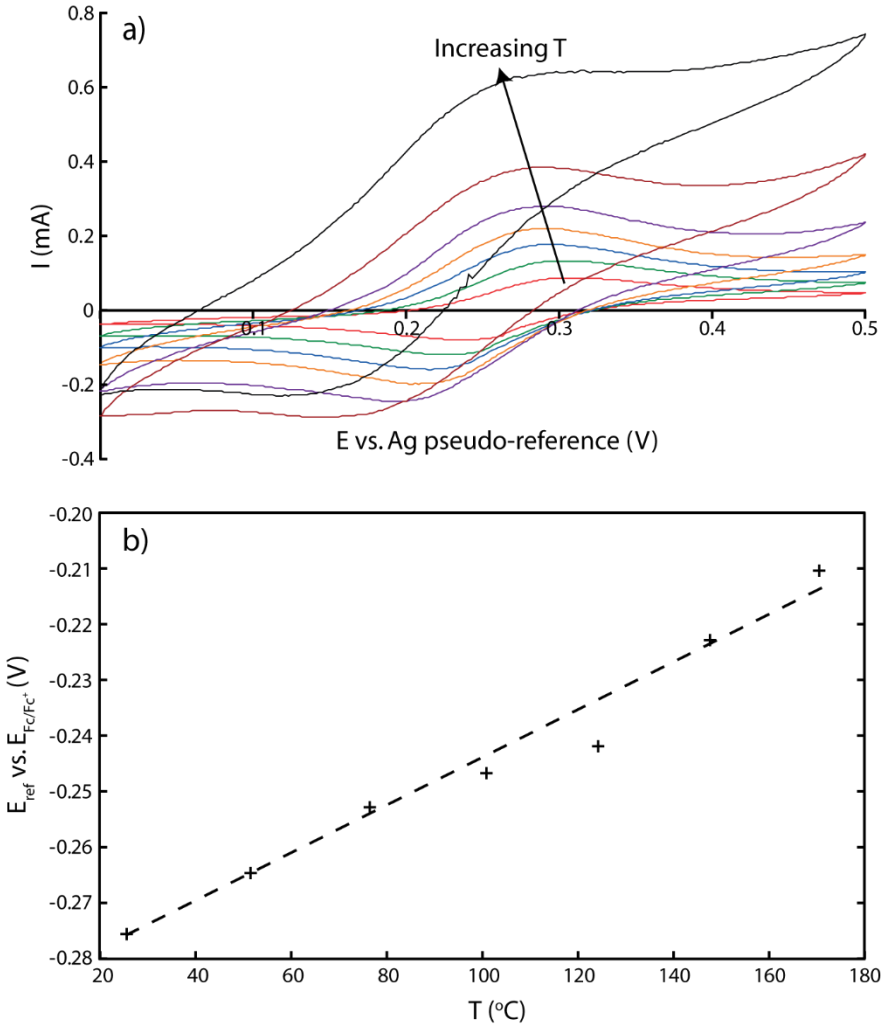

Figure 1: a) Cyclic voltammograms of 10 mM ferrocene in EMIm TFSI measured relative to a Ag wire pseudo-reference electrode, recorded at room temperature and in steps of 25 °C between 50 °C and 175 °C with a sweep rate of 10 mV/s. b) The potential of the Ag pseudo-reference electrode at each temperature, measured relative to the ferrocene/ferrocenium couple, as determined from the average of the peak potentials in the cyclic voltammograms.

2 DFT Calculations

The correlated nature of the electrons in VO_2 makes the use of DFT to calculate the electronic structure challenging, and a number of approaches have previously been applied to accurately study VO_2, including Hubbard U corrections,[2] hybrid functionals[3] and dynamical mean field theory.[4] However,

calculations of magnetic resonance properties using the Gauge Including Projector Augmented Waves (GIPAW) method are either too computationally expensive or not currently implemented with these methods; instead, for the purposes of spectral assignment and estimation of quadrupolar parameters, a generalised gradient approximation (GGA) approach was used here.

DFT calculations of NMR parameters were performed using the CASTEP plane wave density functional theory (DFT) code[5–8] and the PBE exchange-correlation functional,[9] with a plane wave cut-off energy of 700 eV and a 6 × 6 × 6 Monkhorst−Pack *k*-point mesh. The relationship between the calculated chemical shielding and the experimental chemical shift was determined by calculating the isotropic value of the ^{17}O NMR shielding tensor for selected diamagnetic binary first-row transition metal oxides—Sc_2O_3, rutile TiO_2 and V_2O_5 (the last of which has three different oxygen sites)—and plotting this against the experimental isotropic chemical shift[10] (Figure 2). The atomic positions and unit cell parameters were relaxed from the experimental structures, which were taken from ICSD entries 26841,[11] 62677[12] and 15798,[13] respectively.

The calculation of the NMR parameters in monoclinic, insulating, VO_2 was performed using the experimental XRD structure (ICSD entry 34033[14]). The structure was relaxed using a Hubbard U correction of 0.5 eV to account for the electron correlations and stabilise the insulating structure, then the NMR parameters were calculated without the Hubbard U but with fixed electronic occupancy so as to retain the insulating ground state. Table 1 shows the calculated ^{17}O chemical shifts, converted from shielding values using the regression of Figure 2; although the exact agreement with the experimental values is not excellent, the difference between the two oxygen environments is clear, enabling their assignment. Shown also are the quadrupolar coupling constants of the two environments, which were converted to the second-order quadrupolar shifts expected at 7.05 T using the MagresView software package.[15]

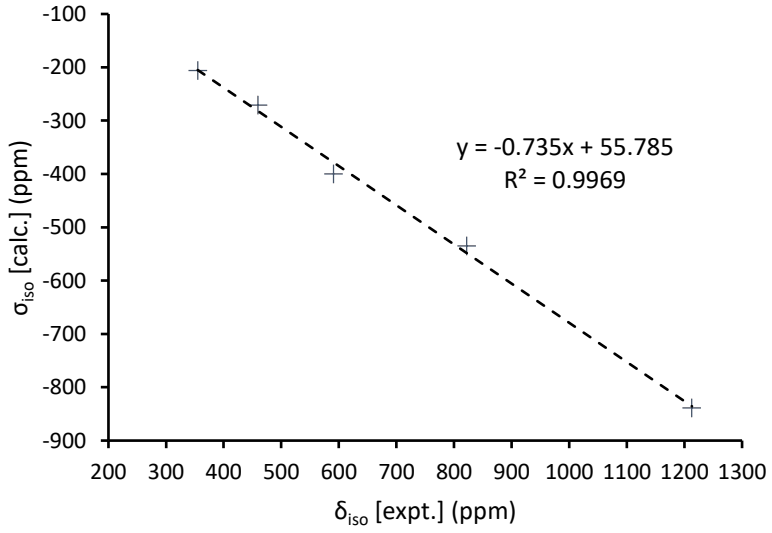

Figure 2: Calculated ^{17}O NMR isotropic shielding values plotted against the experimental isotropic chemical shift for selected diamagnetic binary first-row transition metal oxides.

Table 1: Calculated and experimental ^{17}O chemical shifts in monoclinic, insulating, VO_2 as well as the calculated quadrupolar coupling constants, C_Q, and resultant second-order quadrupolar shifts at 7.05 T.

	Experimental Shift /ppm	Calculated Shift /ppm	Calculated C_Q /MHz	Second order quadrupolar shift /ppm
Inter-dimer	753	696	1.72	−12
Intra-dimer	814	832	1.56	−10

3 Thermogravimetric Analysis

The hydrogen content of Pd/H_xVO_2 was determined from the mass change due to loss of H_2O on heating the sample to 600 °C in flowing N_2 using a Mettler Toledo TGA/SDTA 851 thermobalance with a 100 µL Al_2O_3 crucible (Figure 3), according to the following equation:

$$\mathrm{Pd_{0.008}H_{\mathit{x}}VO_2} \rightarrow \mathrm{Pd_{0.008}VO_{\left(2-\frac{\mathit{x}}{2}\right)}} + \frac{\mathit{x}}{2}\mathrm{H_2O}$$

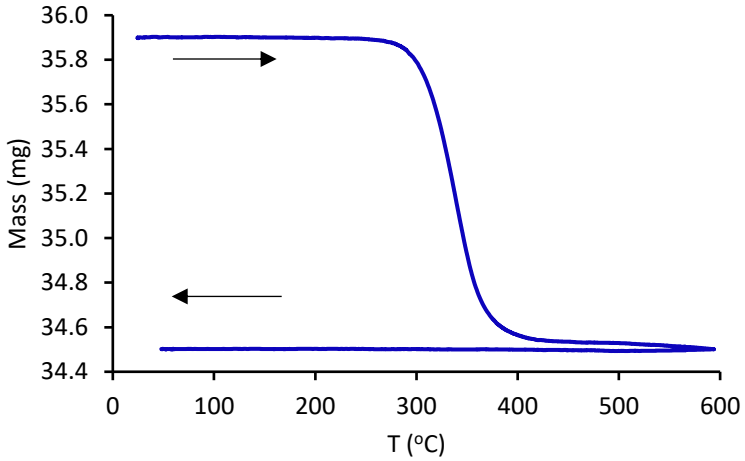

Figure 3: Mass of Pd/H_xVO_2, synthesised at 180 °C, upon heating to 600 °C under flowing N_2.

4 Rietveld Analysis

Figures 5 to 11 show the powder XRD patterns of selected H_xVO_2 samples, the identified phases and the Rietveld refinements. The purpose of the analysis is to identify the phases present and quantify the phase fractions, but the data is of insufficient quality for a full refinement of the atomic positions and displacement parameters and this was not attempted; these are the most likely causes of the discrepancies between the Rietveld refinements and the data. The atomic positions were fixed as shown in Table 2.

Table 2: Atomic positions in VO_2 and H_xVO_2.

Phase	Atom	x	y	z
VO_2 M	V	0.240	0.982	0.032
	O	0.106	0.21	0.203
	O	0.416	0.735	0.316
H_xVO_2 O1a & O1b	V	0	0	0
	O	0.279	0.311	0

The zero error was determined for the films from the PTFE reflection at 2θ = 18.21°. A preferred orientation along the [110] direction was observed for the orthorhombic phases and corrected for; although the preferred orientation effect could be removed for the Pd/H_xVO_2 sample by sprinkling the powder on vacuum grease, the signal intensity was then much worse, and this was also not possible for the PTFE films. The lattice parameters and phase fractions were then refined (Table 3).

To determine the hydrogen content of the orthorhombic phases from the cell parameters, the relationship between the orthorhombic distortion and the hydrogen content was determined from the data of Chippindale et al.[16] (Figure 4). The total hydrogen content of the sample could then be predicted by multiplying the hydrogen content of each phase by the phase fraction; the contribution

from the monoclinic phase, if present, cannot be reliably determined from the cell parameters, so is not included in this approach.

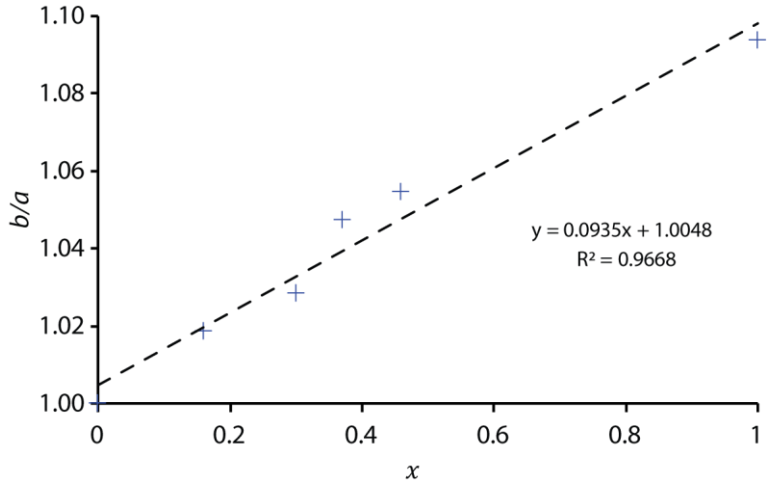

Figure 4: The orthorhombic distortion, b/a, plotted against the hydrogen content, x in H_xVO_2, for the data of Chippindale et al.[16]

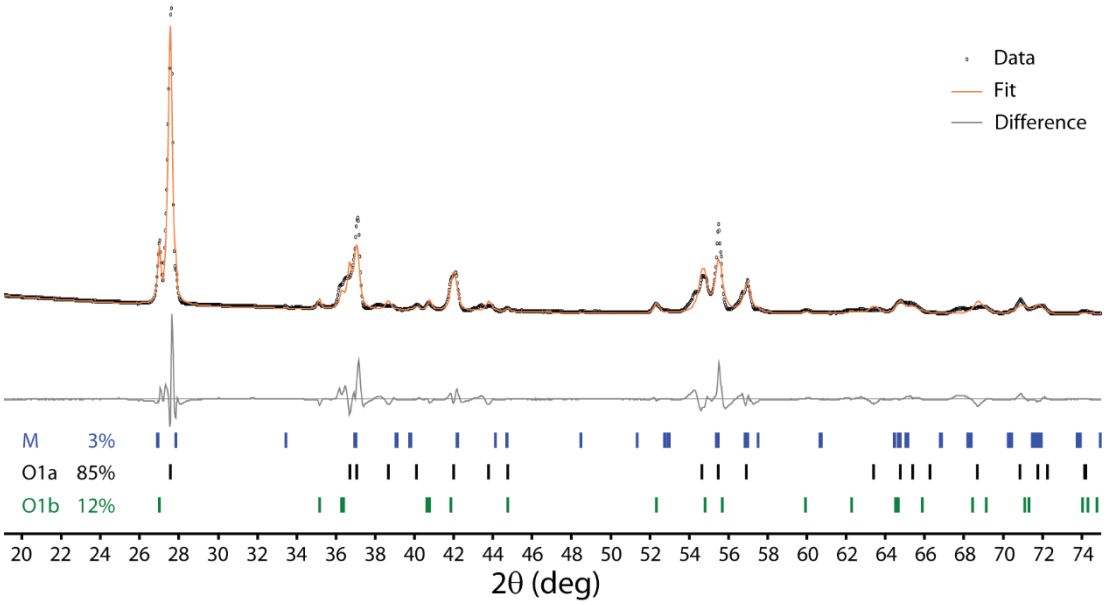

Figure 5: XRD pattern and Rietveld refinement of VO_2 catalytically hydrogenated at 180 °C with 25% H_2/N_2.

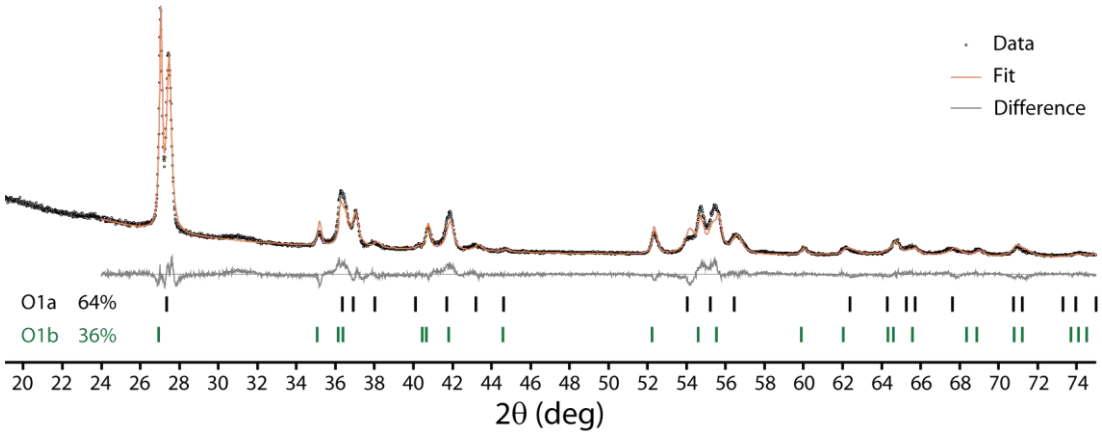

Figure 6: XRD pattern and Rietveld refinement of VO_2 catalytically hydrogenated at 220 °C with 5% H_2/Ar.

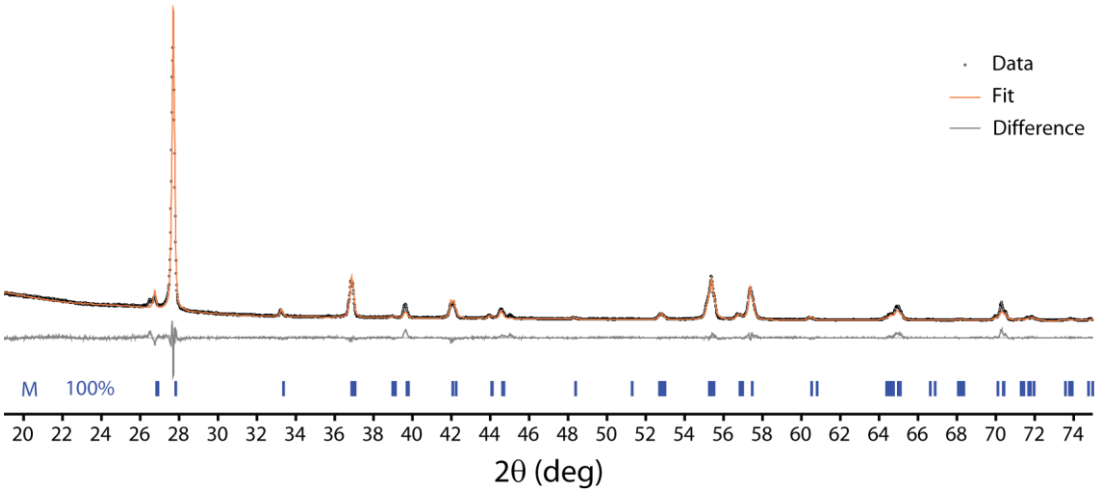

Figure 7: XRD pattern and Rietveld refinement of VO_2 electrochemically hydrogenated at 21 °C.

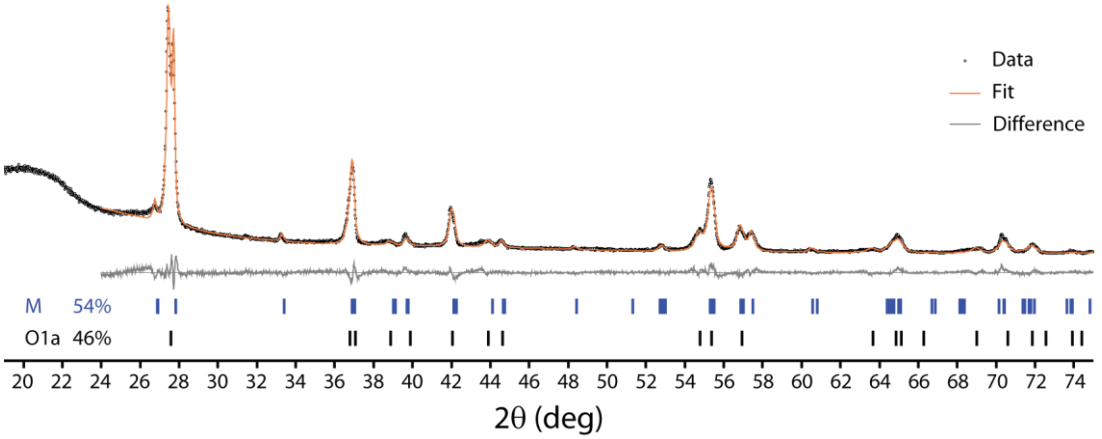

Figure 8: XRD pattern and Rietveld refinement of VO_2 electrochemically hydrogenated at 50 °C .

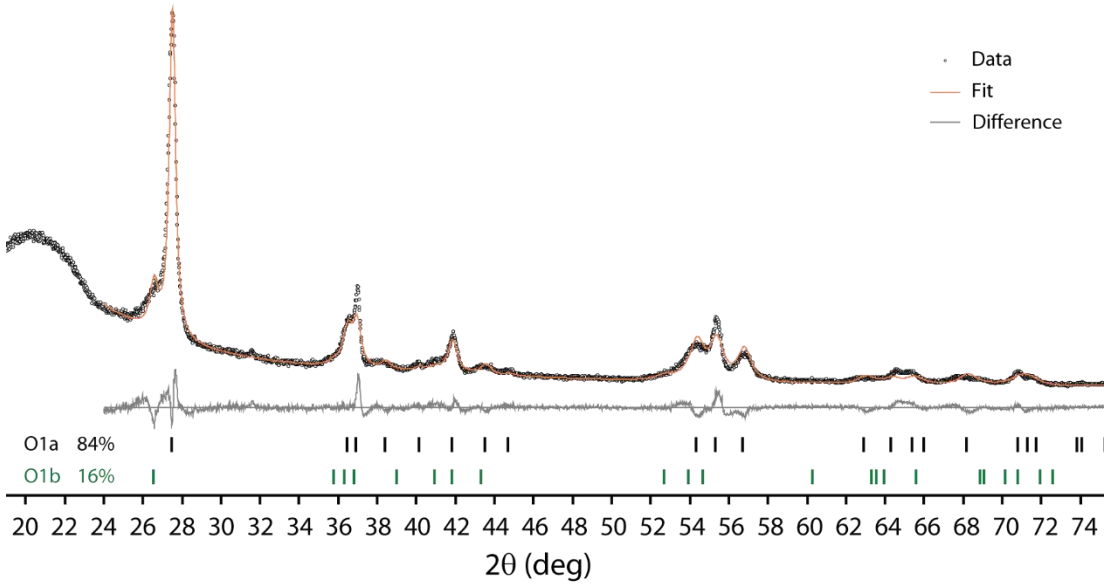

Figure 9: XRD pattern and Rietveld refinement of VO_2 electrochemically hydrogenated at 100 °C

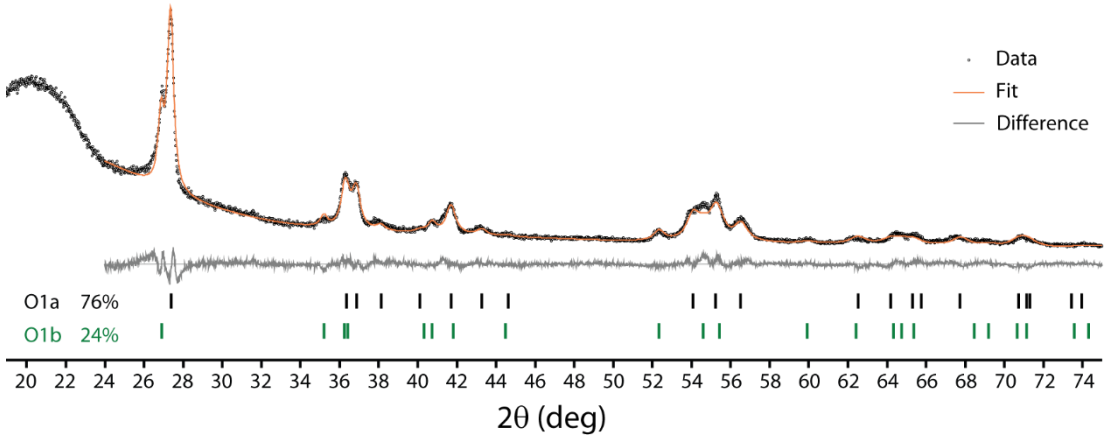

Figure 10: XRD pattern and Rietveld refinement of VO_2 electrochemically hydrogenated at 150 °C.

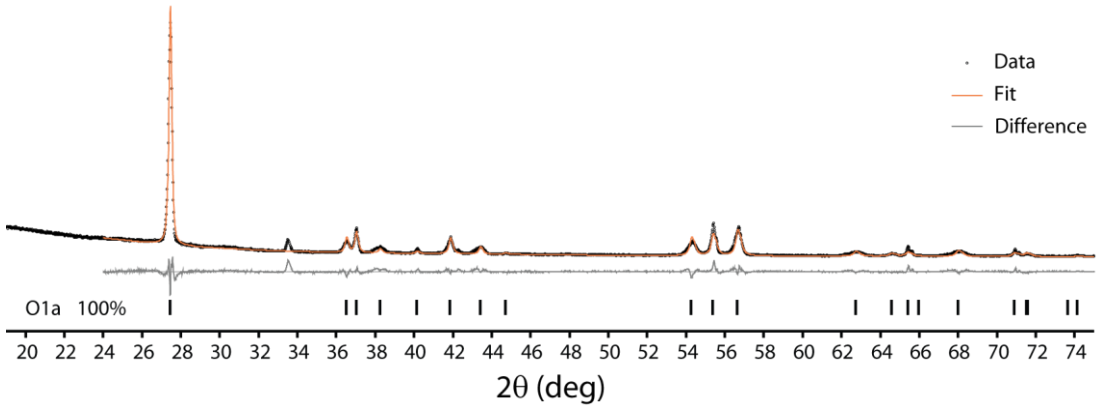

Figure 11: XRD pattern and Rietveld refinement of VO_2 electrochemically hydrogenated at 200 °C. The peak at 2θ = 33.5° is ascribed to an unknown impurity or minor product.

Table 3: Phase fractions and lattice parameters of the monoclinic and two orthorhombic phases in different H_xVO_2 samples, as well as the hydrogen content, x, of the phase as determined from the orthorhombic distortion. The contribution of the phase to the total hydrogen content of the sample, x_{eff}, is found by multiplying the hydrogen content of the phase by its phase fraction, and the total hydrogen content of the sample, x_{tot}, is then predicted by summing the contributions from each phase.

		Pristine VO_2	**Catalytic Hydrogenation**		**Electrochemical Hydrogenation**				
			180 °C 25% H_2	220 °C 5% H_2	21 °C	50 °C	100 °C	150 °C	200 °C
M	wt%	100%	2.6%		100%	54.1%			
	a	5.753	5.753		5.756	5.755			
	b	4.526	4.526		4.527	4.526			
	c	5.383	5.383		5.384	5.380			
	β	122.6	122.6		122.6	122.6			
O1a	wt%		85.5%	64.2%		45.9%	83.5%	75.6%	100.0%
	a		4.494	4.494		4.515	4.491	4.494	4.489
	b		4.654	4.729		4.631	4.688	4.718	4.704
	c		2.877	2.895		2.874	2.895	2.899	2.885
	x		0.329	0.508		0.224	0.417	0.484	0.462
	x_{eff}		0.280	0.326		0.103	0.348	0.366	0.462
O1b	wt%		11.9%	35.8%			16.5%	24.4%	
	a		4.444	4.455			4.545	4.470	
	b		4.941	4.935			4.944	4.930	
	c		2.981	2.990			2.895	2.974	
	x		1.144	1.103			0.889	1.051	
	x_{eff}		0.153	0.395			0.147	0.256	
Total	x_{tot}		0.433	0.721		0.103	0.495	0.622	0.462

Figure 12 shows a comparison of the hydrogen contents determined by quantitative ^{1}H NMR and Rietveld analysis of the powder XRD patterns. The positive correlation supports the assignment of the lower and higher shift regions of the ^{1}H NMR spectrum to the O1a and O1b phases respectively, and the use of the orthorhombic distortion to predict the hydrogen content from the unit cell parameters. However, there is also both scatter in the values greater than the predicted uncertainty as well as systematic deviation. The scatter is most likely due the difficulty in accurately determining the phase fractions from Rietveld analysis with broad peaks, as small changes in amplitude correspond to large changes in mass fraction. The quantitative ^{1}H NMR also generally predicts a lower hydrogen content than the XRD analysis; this is most likely due to NMR skin depth effects: the metallic nature of the samples reduces radiofrequency penetration so that the sample is not fully excited and the ^{1}H NMR signal is reduced. This was be circumvented for the catalytically hydrogenated Pd/H_xVO_2 samples by grinding with KBr, and for these samples, the NMR and XRD determined hydrogen contents are in better agreement. However, for the electrochemically hydrogenated VO_2, the PTFE films could not be ground with KBr, and although the presence of PTFE reduces the skin depth effect, there is still a notable contribution. It can also be seen that the skin depth effect mostly contributes to the metallic O1a phase, rather than the paramagnetic O1b phase.

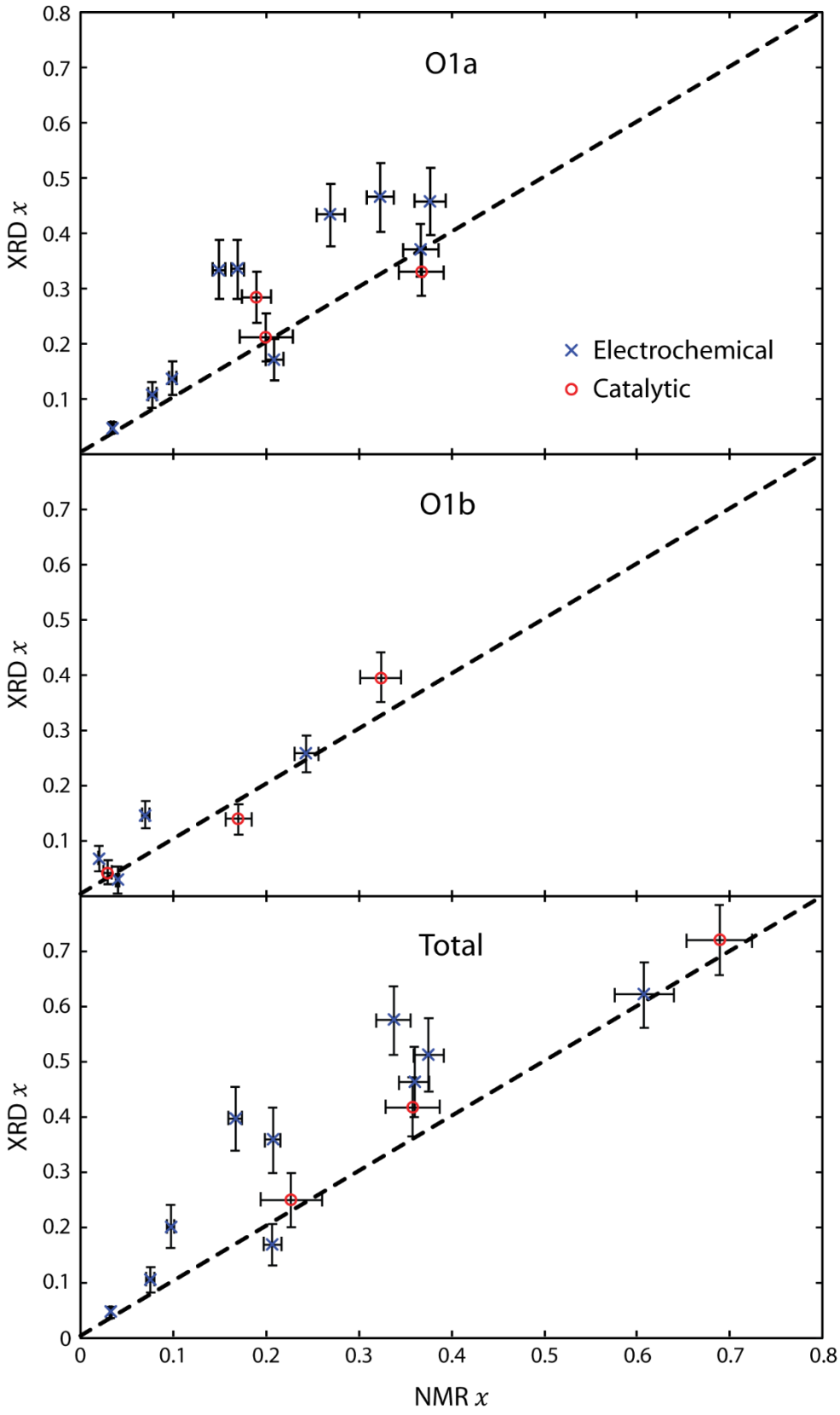

Figure 12: Comparison of the hydrogen content of each orthorhombic phase and the total hydrogen content for various H_xVO_2 samples as determined by quantitative ^1H NMR and by the unit cells and phase fractions from Rietveld refinement of the powder XRD patterns. The dashed line indicates 1:1 agreement between the methods.

5 ^{1}H NMR of Different Catalytically Hydrogenated Samples

Two samples of VO_2 were catalytically hydrogenated, one using 25% H_2/N_2 at 180 °C and one using 5% H_2/Ar at 220 °C. Rietveld analysis of the former gave a ratio of the two orthorhombic phases O1a:O1b of 85:12 compared to 64:36 for the latter (Figure 5, Figure 6 and Table 3). The ^{1}H NMR spectra of the two samples are shown in Figure 13; the second sample has a much higher ratio of the signal at 450 ppm to that at 100 ppm, suggesting that the two shift regions correspond to the O1b and O1a phases respectively. This assignment is supported by the quantitative analysis of many samples, both electrochemically and catalytically hydrogenated (Figure 12).

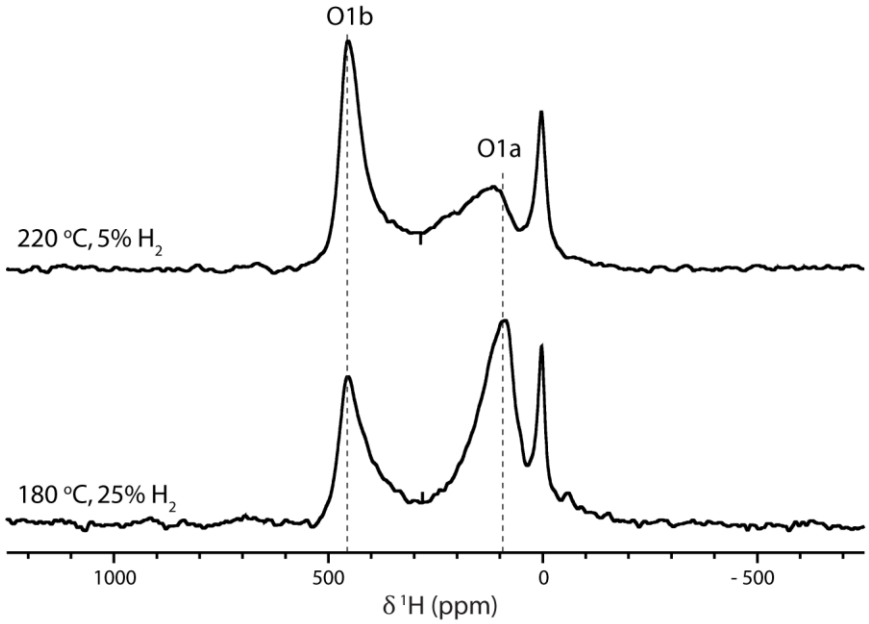

Figure 13: ^{1}H NMR spectra of catalytically hydrogenated VO_2 samples prepared via *two different procedures. The spectra were recorded at 4.70 T and 40 kHz MAS using a MATPASS sideband separation pulse sequence and taking the isotropic slice.*

6 Variable Temperature ^{1}H NMR

Figure 14 shows the ^{1}H MATPASS NMR spectra of Pd/H_xVO_2 between 18 °C and 69 °C. The sample was ground with KBr so that the sample temperature could be determined *in-situ* by the temperature-dependent KBr T_1 constant and chemical shift.[17] The O1a peak appears to move to higher frequency with increasing temperature, but this is actually due to the lower frequency regions relaxing more quickly at higher temperatures and hence less of this signal being observed relative to the higher frequency regions; this effect makes it challenging to determine whether the chemical shifts are temperature-dependent, but the chemical shift certainly does not decrease with increasing temperature, ruling out a paramagnetic shift. The O1b shift, on the other hand, does decrease with increasing temperature; to determine whether this shift followed the expected Curie–Weiss temperature dependence, a wider temperature range was explored using a 4 mm rotor with a zirconia cap, again with an *in-situ* KBr thermometer. A single pulse experiment was used because the lower maximum spinning speed of 14 kHz, for the larger rotor, and fast T_2 relaxation of the sample prevented rotor synchronised experiments such as a MATPASS or a Hahn echo; the background in the single pulse experiment then obscured the O1a signal so that only the O1b signal could be distinguished. Figure 15a shows a plot of 1/shift versus temperature for the O1b signal, which shows the expected linear Curie–Weiss dependence, confirming that this is a paramagnetic shift, which is positive due to the 90° π delocalisation pathway (Figure 15b).

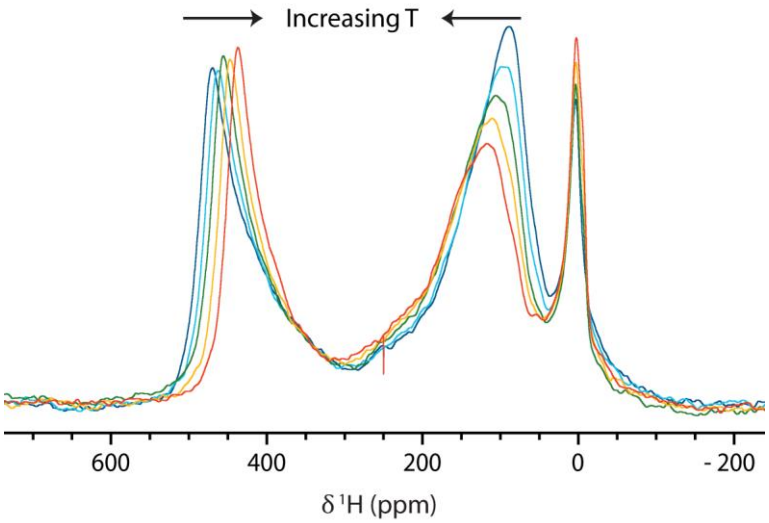

Figure 14: Variable temperature ^{1}H MATPASS NMR (7.05 T) spectra at 60 kHz MAS with sample temperatures between 18 °C and 69 °C as determined from the in-situ KBr NMR thermometer.

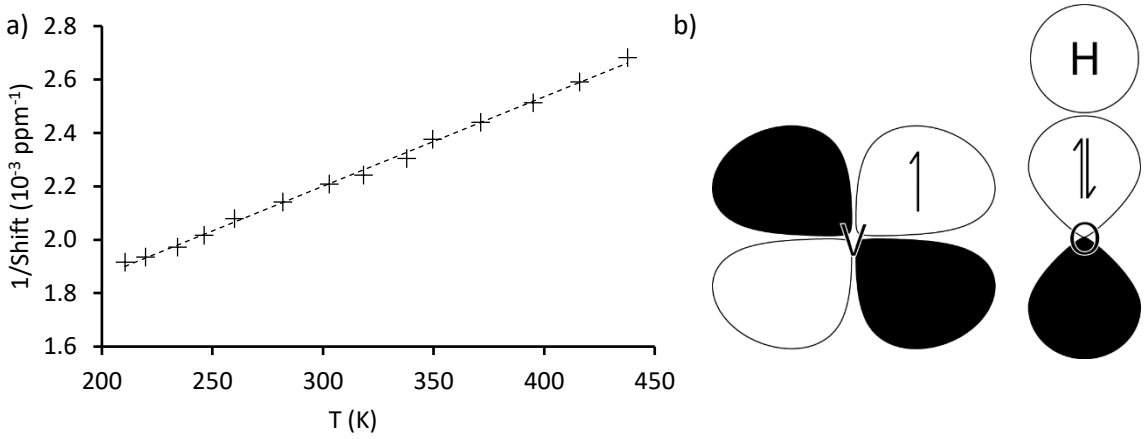

Figure 15: a) A plot of 1/shift against T for the ^{1}H O1b shift in Pd/H_xVO_2. The spectra were recorded using a single-pulse experiment at 14 kHz MAS and 4.70 T. The sample temperature was determined with an in-situ KBr NMR thermometer. b) Schematic representation of the 90° π delocalisation pathway which gives a positive paramagnetic shift on the proton.

7 ^{1}H T_1 measurements

To measure the T_1 relaxation constant for the ^{1}H environments in H_xVO_2, an inversion recovery experiment was used. Both the O1a and O1b NMR signals represent a distribution of environments, but this can be modelled reasonably well by deconvoluting the signal from each phase as two Gaussian-Lorentzian peaks, as shown in Figure 16 for the MATPASS ^{1}H spectrum. This permits the contribution from each signal to be determined in the ^{1}H inversion recovery spectra as a function of the relaxation time (Figure 17), which in turn can be fitted to find the T_1 relaxation constants (Table 4). The relaxation is fast for both phases due to the metallic and paramagnetic environments (the T_1 constants of diamagnetic protons in insulating environments are typically 1–10 s), with the paramagnetic relaxation of the O1b signals an order of magnitude faster than that of the O1a signals, further supporting the assignment of the O1b signal as paramagnetically shifted. Furthermore, within the signal of each phase, the component with a higher shift has a shorter relaxation constant; this is as expected because a higher shift corresponds to a more metallic or more paramagnetic environment respectively, for which the relaxation is consequently faster.

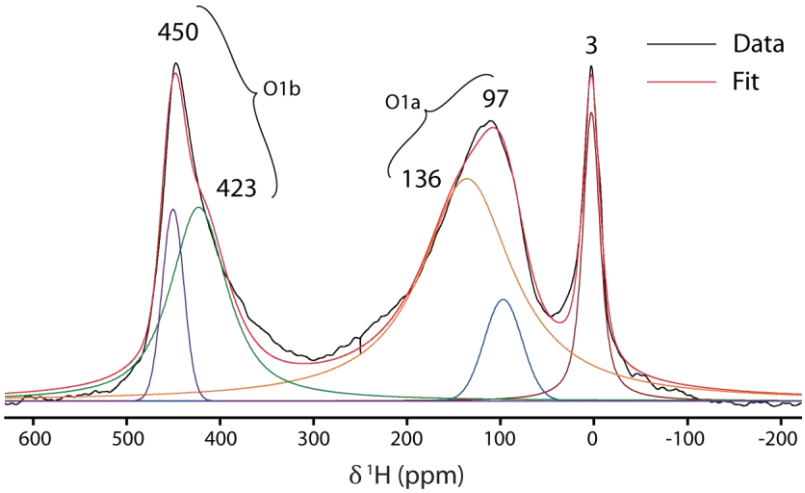

Figure 16: Gaussian-Lorentzian deconvolution of the ^{1}H MATPASS NMR spectrum of catalytically hydrogenated Pd/H_xVO_2, recorded at 7.05 T and 60 kHz MAS.

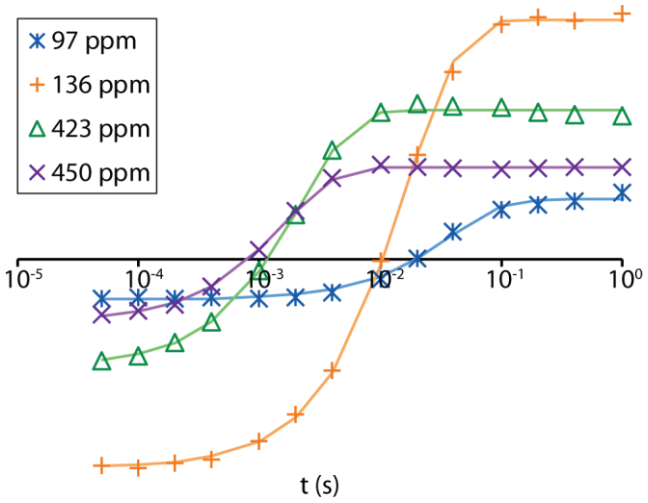

Figure 17: Intensity as a function of relaxation time for different environments in the ^{1}H inversion recovery NMR spectra of catalytically hydrogenated Pd/H_xVO_2.

Table 4: Fitted T_1 relaxation constants for different environments from the ^{1}H inversion recovery NMR spectra of catalytically hydrogenated Pd/H_xVO_2.

	97 ppm	**136 ppm**	**423 ppm**	**450 ppm**
T_1**/s**	0.039	0.017	0.0022	0.0016

8 Magnetisation *vs.* Field Measurements

Figure 18 shows the magnetisation *vs.* field measurements for VO_2 electrochemically hydrogenated at room temperature, recorded below (60 K) and above (300 K) the spin glass freezing temperature ($T_f \approx$ 150 K). Below T_f there is hysteresis in the magnetisation about the origin, which is no longer present above T_f; this is characteristic of a spin glass-like state.[18]

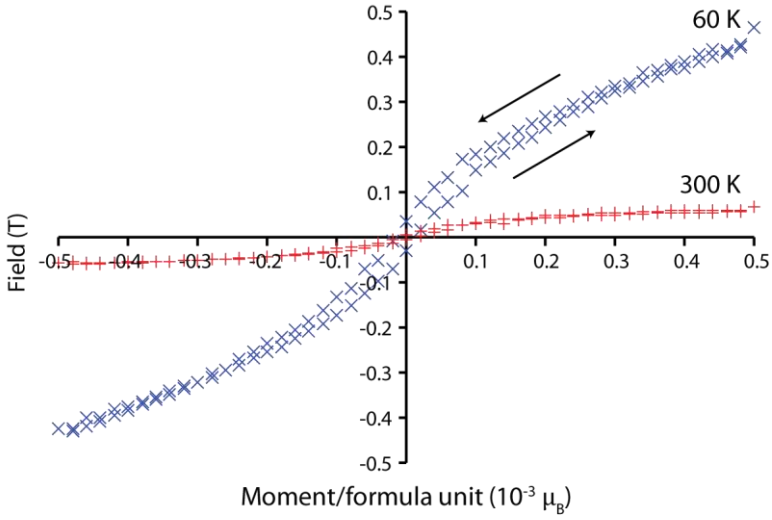

Figure 18: M(H) curves for VO_2 electrochemically hydrogenated at room temperature, recorded below (60 K) and above (300 K) the spin glass freezing temperature (T_f).

9 Comparison of the ^{17}O NMR of Pristine and Electrochemically Hydrogenated VO_2

Figure 19 shows the ^{17}O NMR spectra of ^{17}O enriched VO_2 recorded above the MIT, before and after electrochemical hydrogenation with EMIm TFSI ionic liquid at room temperature. The two peaks from residual monoclinic insulating VO_2, present due to the finite width of the MIT and temperature gradients in the rotor, are at the same shift for both samples. However, the signal from metallic rutile VO_2 is shifted to more negative frequency for the electrochemically hydrogenated samples; this is evidence of the electron doping associated with hydrogen intercalation, which increases the density of states at the Fermi level, and hence the Knight shift.

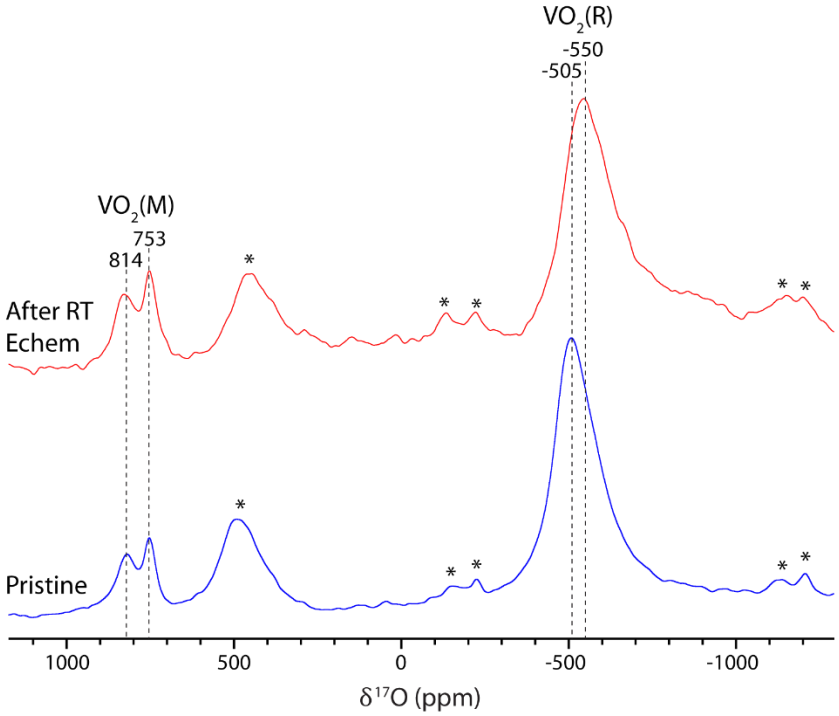

Figure 19: ^{17}O NMR spectra of ^{17}O-enriched VO_2 above the MIT, before and after electrochemical hydrogenation with EMIm TFSI at room temperature, showing metallic rutile VO_2(R) and residual insulating monoclinic VO_2(M). Spectra were recorded at 69 °C, 7.05 T and 40 kHz MAS using a Hahn echo pulse sequence; sidebands are marked with an asterisk.

10 Two-Electrode Potentiostatic Electrochemical Hydrogenation

Figure 20a shows the current and specific charge profiles for bulk VO_2 potentiostatically hydrogenated by applying −2.5 V between the Pt counter electrode and VO_2 working electrode for 11 hours, while Figure 20b shows the subsequent ^{1}H NMR spectrum. The H_xVO_2 signal is clearly observed in the ^{1}H NMR, indicating that hydrogenation has occurred, while quantification yields x = 0.016, which corresponds to a specific charge of 5.2 mAh g^{-1}. The current rapidly decays then approaches a non-zero value of ~0.01 mA; the charge required for hydrogenation has been transferred within the first 30 minutes, so the subsequent and limiting current correspond to electrolyte breakdown, which is still appreciable even with an applied voltage of 2.5 V.

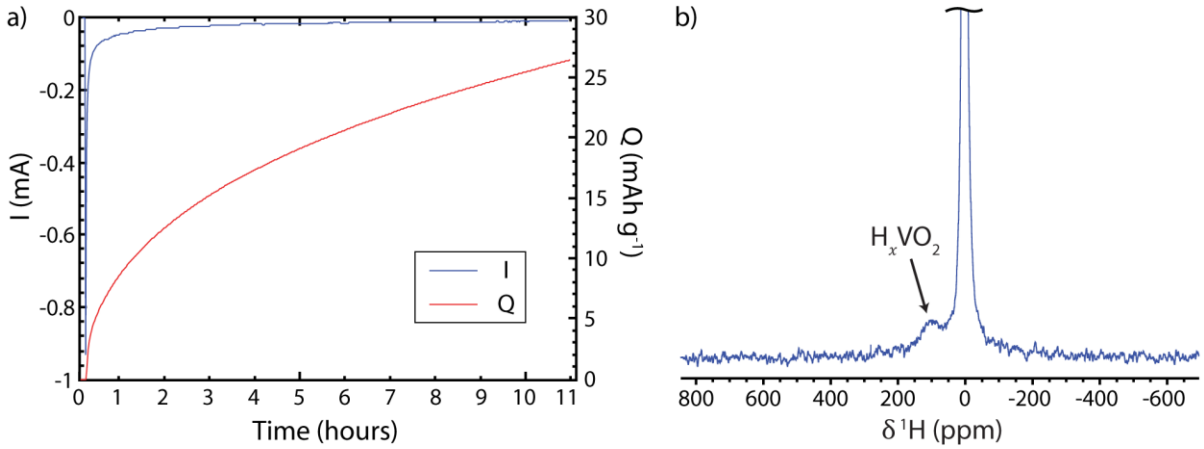

Figure 20: a) Current and specific charge profiles and b) ^{1}H NMR spectrum of potentiostatically hydrogenated VO_2. The spectrum was recorded at 40 kHz MAS and 4.70 T, taking the isotropic slice from a MATPASS spectrum.

11 Reversible Electrochemical Hydrogenation

To test the reversibility of electrochemical hydrogenation, a bulk VO_2 sample was galvanostatically reduced for 24 hours at room temperature with EMIm TFSI, before reversing the current for 24 hours (Figure 21a). The ^{1}H spectrum for this sample (Figure 21b) shows only the diamagnetic signal and the broad probe background, but no H_xVO_2 signal, indicating that the hydrogenation has been reversed. Closer examination of the voltage profile shows that during reduction the potential of the VO_2 working electrode reaches a limiting plateau, with only the initial sloping region corresponding to hydrogenation of VO_2. When the current is switched to VO_2 oxidation, the working electrode potential increases again while the VO_2 dehydrogenates, before reaching a limiting potential corresponding to the anodic limit of the ionic liquid – at approximately the same potential observed at the Pt counter electrode during reduction. Notably, however, on oxidation the potential of the Pt counter electrode is significantly lower than observed at the VO_2 electrode during its reduction: this indicates that the cathodic stability of the ionic liquid is decreased at a VO_2 electrode relative to a Pt electrode, possibly explaining why electrolyte breakdown reactions are significant in this system at voltages which are within the typically reported stability window.

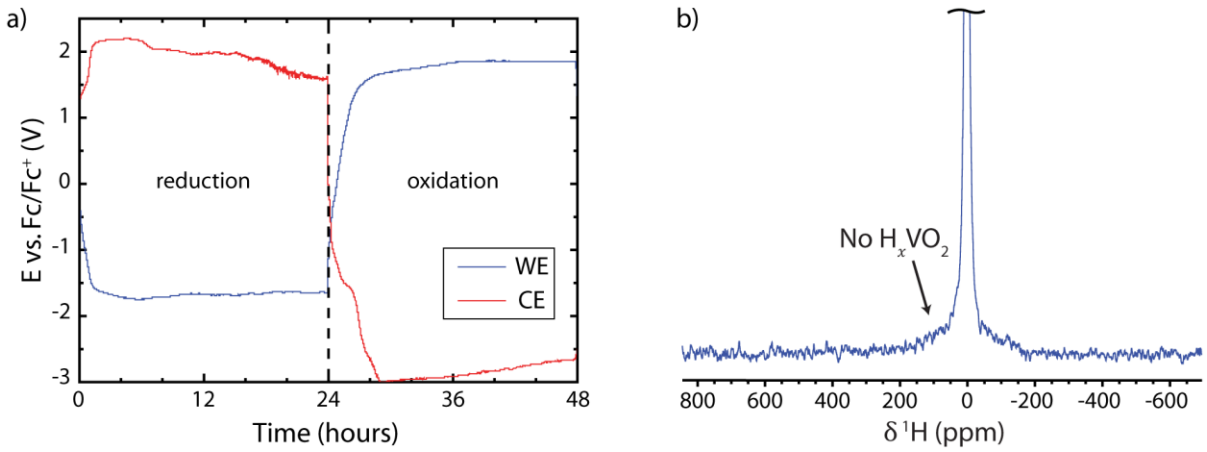

Figure 21: a) Voltage profiles for the VO_2 working electrode (WE) and Pt counter electrode (CE), and b) ^1H NMR spectrum of reversibly electrochemically hydrogenated VO_2. The spectrum was recorded at 40 kHz MAS and 4.70 T with a MATPASS pulse sequence.

12 SEM of Bulk VO_2

Figure 22 shows a representative SEM micrograph of a bulk VO_2 film, made with 10 wt% PTFE binder and 10 wt% conductive carbon nanoparticles. Analysis of 100 particles using ImageJ gives an average particle size of 1.9 µm, with a standard deviation of 0.9 µm.

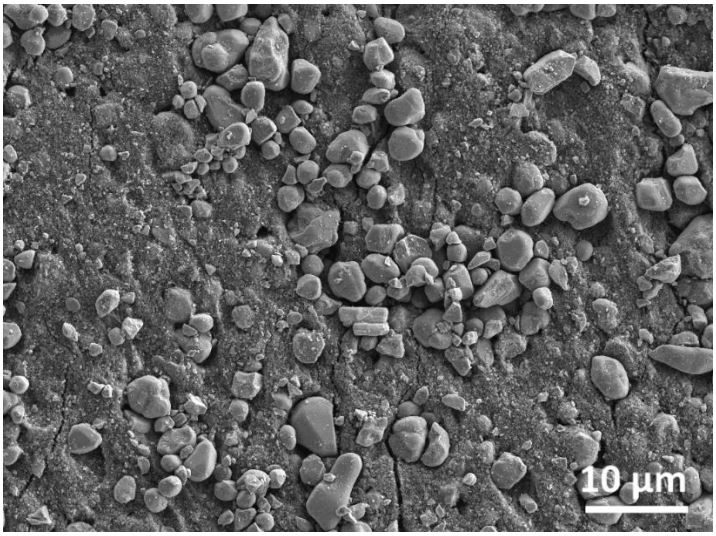

Figure 22: SEM micrograph of bulk VO_2 with 10 wt% PTFE and 10 wt% conductive carbon nanoparticles.

13 Electrochemical Hydrogenation of VO_2 Nanoparticles

To determine whether electrochemical hydrogenation of bulk VO_2 at room temperature was limited by the particle size, VO_2 nanoparticles were synthesised by ball milling. The comproportionated VO_2 (500 mg) was ball milled for 8 × 15 minutes in a 50 mL zirconia jar with five 10 mm diameter zirconia balls, using a Fritsch Pulverisette 23 shaker mill. The resultant nanoparticles were then characterised *via* powder XRD, SEM and scanning transmission electron microscopy (STEM). Analysis of the XRD peak widths yielded an average crystallite size of 12 nm, however this is an underestimate as it ignores any broadening due to strain. The electron microscopy (Figure 23) reveals micron-sized secondary particles, comprising primary particles averaging 30 nm in diameter, with particles as small as 10 nm being distinguishable in the STEM image.

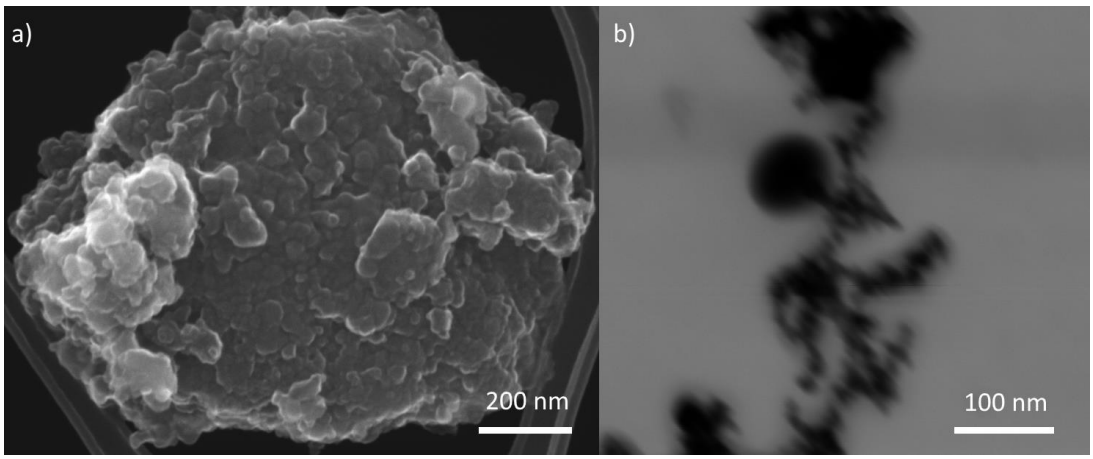

Figure 23: a) SEM image of ball-milled VO_2 nanoparticles, showing a larger secondary particle comprising smaller primary particles, and b) STEM image showing some unagglomerated primary particles.

From the VO_2 nanoparticles, a composite free-standing film was made with 10% PTFE and 10% conductive carbon. The film then underwent galvanostatic electrochemical reduction at room temperature (Figure 24). The voltage profile exhibits a less steep gradient than for bulk VO_2 and more charge is transferred before hitting the limiting plateau at around −1.6 V. The ^{1}H NMR spectrum (Figure 25a) shows greater hydrogenation, and quantification yields a hydrogen content of $x = 0.20$, *c.f.* 0.037 for bulk VO_2; the hydrogen content also matches well with the amount of charge transferred before reaching the limiting plateau. The ^{51}V NMR spectrum (Figure 25b) does show a broad signal at negative shift due to vanadium in a metallic environment, however some of the signal from insulating VO_2(M) remains. Some side products are also evident, with the same diamagnetic vanadium signal as observed after electrochemical reduction of bulk VO_2 at 100 °C and 150 °C. The lack of uniform metallisation in this case is ascribed to the difficulty of electrically contacting all the nanoparticles with the conductive carbon, which is compounded by the presence of secondary agglomerates; it is likely that some particles are electrically or electrochemically isolated and hence are not reduced, giving rise to the residual VO_2(M) signal. Nevertheless, the greater hydrogenation observed for nanoparticulate VO_2 as compared to bulk VO_2 suggests that particle size is the reason full metallisation is not observed for the latter. This is most likely due to sluggish kinetics of hydrogen diffusion and/or nucleation and growth of the new phases, relative to competing electrochemical side reactions such as hydrogen evolution.

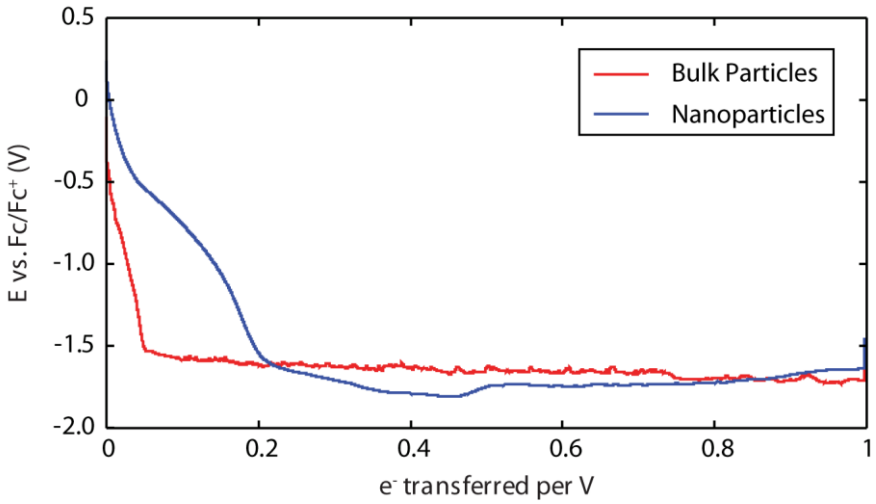

Figure 24: Voltage profiles for bulk (~2 µm) and nanoparticulate (~30 nm) VO_2 electrochemically reduced at room temperature with EMIm TFSI.

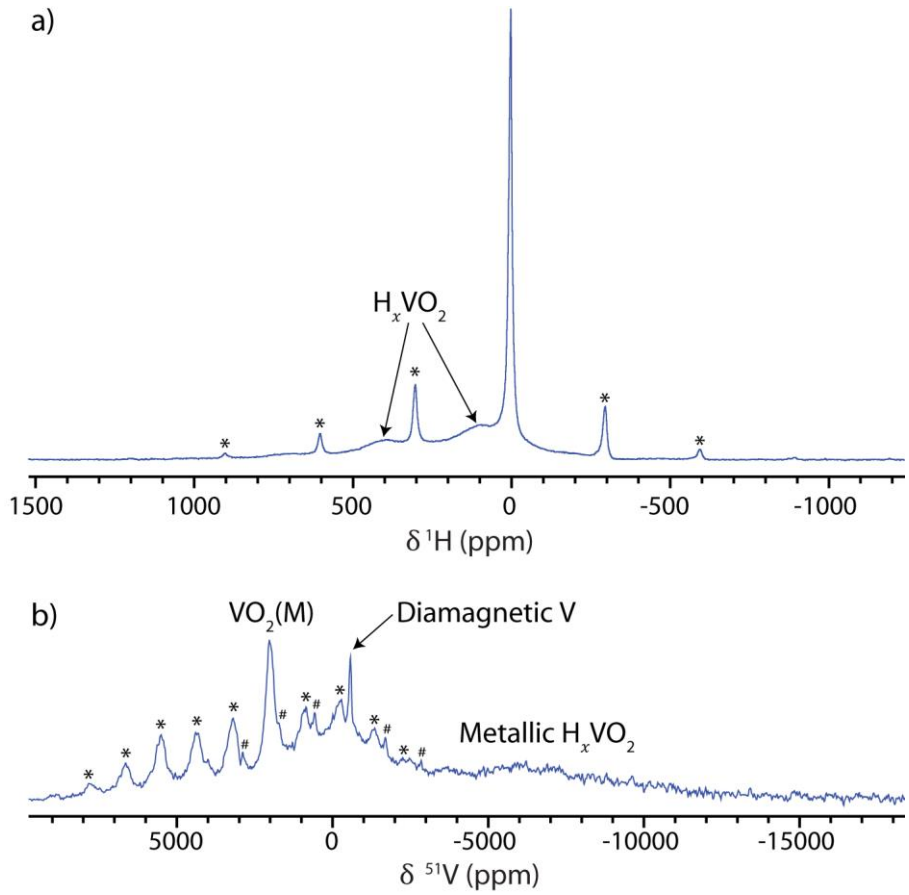

Figure 25: a) ^{1}H and b) ^{51}V NMR spectra of electrochemically hydrogenated VO_2 nanoparticles, recorded at 4.70 T and 60 kHz MAS using a Hahn echo pulse sequence. The ^{51}V spectrum was acquired in steps of 5000 ppm between carrier frequencies of 5000 ppm and −20000 ppm and summed to produce the spectrum shown above. Spinning sidebands are marked with asterisks or hash marks.

14 Magnetic Susceptibility Measurements of H_xVO_2 Electrochemically Hydrogenated at Elevated Temperatures

Figure 26 shows the bulk magnetic susceptibility measurements for pristine VO_2 and H_xVO_2 which has been electrochemically metallised between 21 °C and 200 °C. The general trend is an increase in both the Pauli (high T asymptote) and Curie–Weiss (low T tail) paramagnetism with increasing temperature up to 150 °C, due to the increased hydrogenation (main text, Figure 5). The loss of the MIT can also be seen for electrochemical hydrogenation above 50 °C. A maximum in the susceptibility, corresponding to antiferromagnetic ordering, is observed for the samples metallised at the highest three temperatures, at Néel temperatures of ∼8 K for the 100 °C and 150 °C samples and ∼25 K for the 200 °C sample; see section 17 for a discussion of the 200 °C sample. The fit of the Curie–Weiss paramagnetic component from the main text used only points above the Néel temperature.

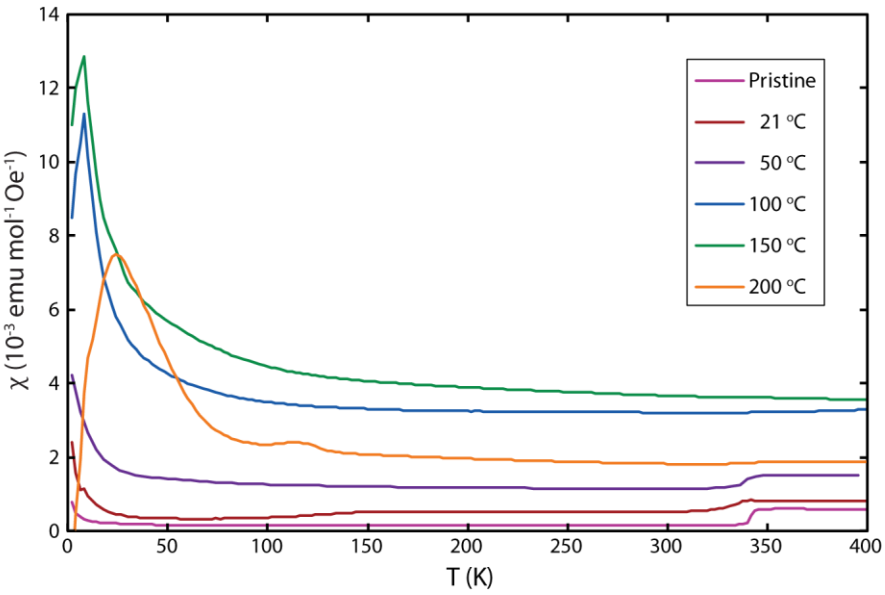

Figure 26: ZFC magnetic susceptibility measurements of pristine VO_2 and H_xVO_2 which has been electrochemically metallised between 21 °C and 200 °C.

15 ^{17}O NMR Spectra of H_xVO_2 Electrochemically Hydrogenated at Elevated Temperatures

Figure 27 shows the ^{17}O NMR spectra of H_xVO_2 electrochemically hydrogenated between 50 °C and 200 °C, recorded above and below the MIT temperature. In the low temperature spectrum, the sample which was electrochemically hydrogenated at 50 °C retains the insulating monoclinic VO_2 signals at 753 and 814 ppm, as was also observed for the room temperature sample (main text, Figure 4e). Then in the spectrum recorded above the MIT, the negatively Knight-shifted signal of the metallic phase is again observed at the more negative shift of −550 ppm, compared to −505 ppm for pristine VO_2;in the same way as for room temperature electrochemical hydrogenation, this is evidence of the electron doping associated with hydrogen intercalation, which increases the density of states at the Fermi level, and hence the Knight shift. Moreover, because this is the same shift as was observed for the room temperature sample, this suggests that the degree of hydrogenation of the monoclinic phase is the same for both samples; the 50 °C sample differs in that it also contains the more hydrogenated O1a phase.

For the sample electrochemically hydrogenated at 100 °C, the insulating monoclinic VO_2 signals are no longer present in the low temperature spectrum, nor is the sharp metallic signal observed in the high temperature spectrum; both spectra instead exhibit a very broad signal with unresolved sidebands, centred at ∼−1100 ppm; this can be more readily seen in the MATPASS spectrum (Figure 28, bottom). The shift of this signal is independent of temperature, so can be assigned as the metallic O1a phase with a core-polarisation negative Knight shift. Again, the shift is more negative due to an increase in the density of states at the Fermi level, due to greater doping of electrons, and the width of the signal may indicate a distribution of local environments or doping levels. The signal from the O1b phase cannot be distinguished, possibly because it is too broad; the peaks in the XRD pattern of VO_2 electrochemically metallised at 100 °C are also very broad (Figure 9), suggesting a distribution of lattice parameters or low crystallinity. Based on the appearance of O1a for this 100 °C sample, it is likely that the O1a phase present in the sample hydrogenated at 50 °C is responsible for the broad background observed in the ^{17}O spectra of that sample, both above and below the MIT.

The sample electrochemically hydrogenated at 150 °C shows a sharper signal at ∼−1500 ppm as well as a shoulder at −1200 ppm; again, this can be more easily seen in the MATPASS spectrum (Figure 28,

bottom). The sharp signal exhibits a Curie–Weiss temperature dependence (Figure 29a), so is assigned to the localised paramagnetic O1b phase; the paramagnetic shift is negative due to the polarisation mechanism of the orthogonal V t_{2g} and O 2s orbitals,[19] and becomes less negative with increasing temperature. The shift of the shoulder is independent of temperature and is assigned to the O1a phase, once more with a more negative Knight shift. See Section 17 for a discussion of the 200 °C sample.

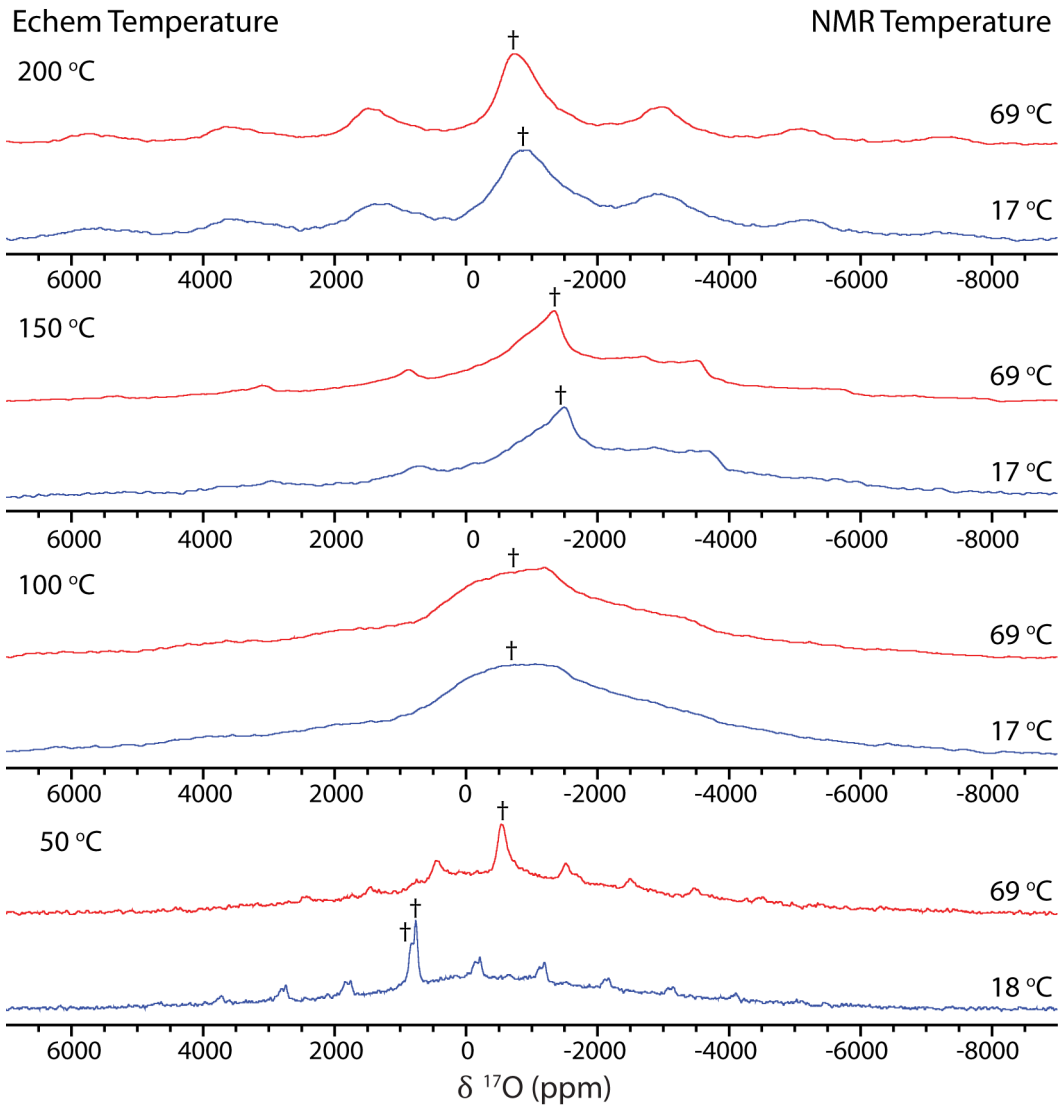

Figure 27: ^{17}O NMR spectra of ^{17}O-enriched H_xVO_2, electrochemically hydrogenated between 50 °C and 200 °C, recorded above and below the VO_2 MIT temperature, using a Hahn echo pulse sequence. The sample electrochemically hydrogenated at 50 °C was recorded at 7.05 T and 40 kHz MAS to afford better resolution of the monoclinic peaks, while the other samples were recorded at 4.70 T and 60 kHz MAS to achieve better sideband separation of the metallic and paramagnetic signals. The isotropic resonances are marked with a dagger.

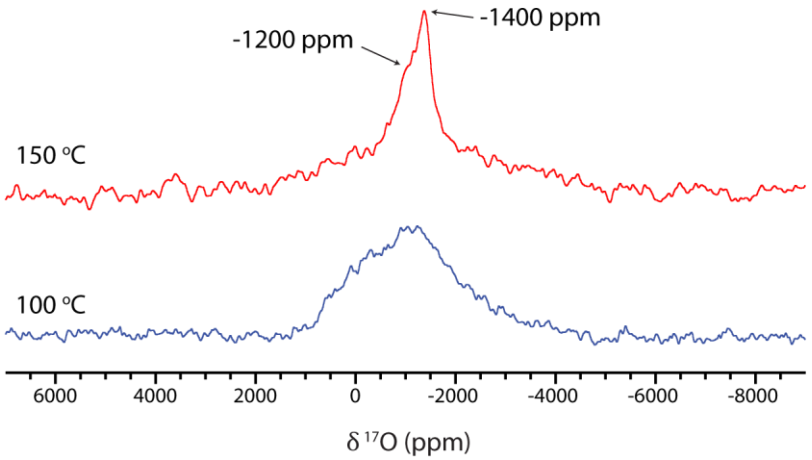

Figure 28: The isotropic slices of the ^{17}O MATPASS NMR spectra of ^{17}O-enriched H_xVO_2 electrochemically hydrogenated at 100 °C and 150 °C. The spectrum of the 100 °C sample was recorded at 7.05 T, 60 kHz MAS and 32 °C; the spectrum of the 150 °C sample was recorded at 4.70 T, 60 kHz MAS and 47 °C.

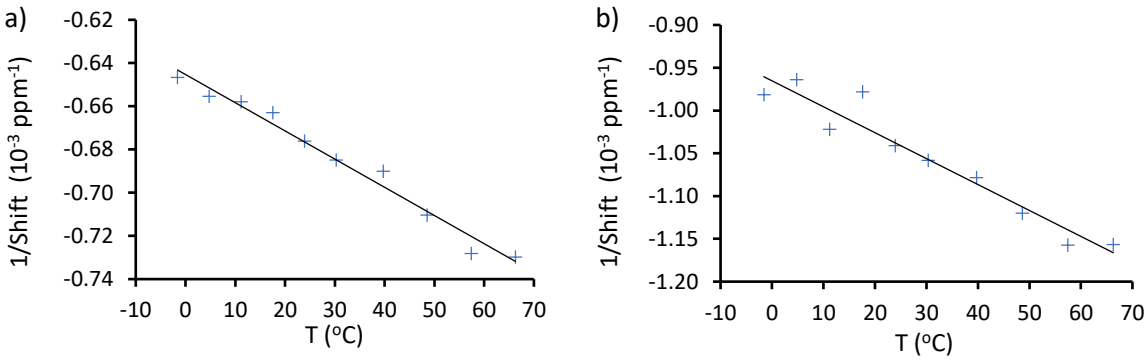

Figure 29: A plot of 1/shift against T for the ^{17}O NMR spectra of ^{17}O enriched H_xVO_2 electrochemically gated at a) 150 °C and b) 200 °C. The spectra were recorded using a Hahn echo at 60 kHz MAS and 4.70 T. The sample temperature was determined by an ex-situ *calibration with the ^{207}Pb signal of $Pb(NO_3)_2$.*

16 Voltage Profiles for Electrochemistry at Elevated Temperatures

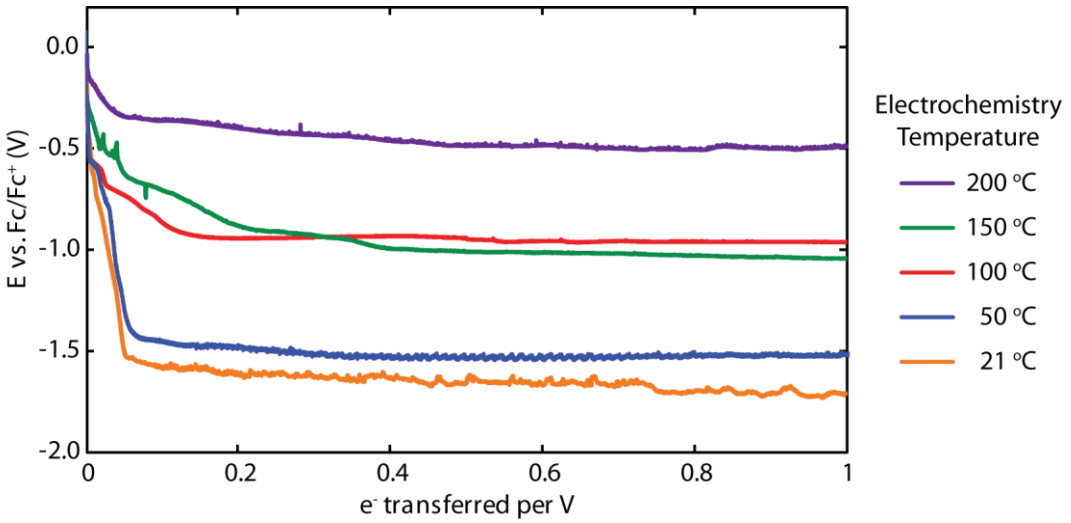

Figure 30: Voltage profiles of electrochemically hydrogenated VO_2 at variable temperature.

17 Electrochemical Metallisation at 200 °C

Electrochemical metallisation of VO_2 at 200 °C affords less hydrogenation than at 150 °C and moreover yields pure O1a, as shown by the XRD pattern (Figure 11) and ^{1}H NMR spectrum (main text, Figure 5c). However, rather than the bulk susceptibility being dominated by the Pauli paramagnetism of the metallic O1a phase, with little of the Curie paramagnetism associated with the O1b phase, the susceptibility actually shows a decrease in the Pauli paramagnetism and the largest Curie constant of all the samples (Figure 26 and main text Figure 5e). This suggests that the O1a phase now contains localised paramagnetic defects.

The ^{17}O NMR spectra recorded after electrochemical metallisation of an isotopically enriched sample at 200 °C support this conclusion (Figure 27). A signal is observed at ∼−800 ppm which exhibits a Curie–Weiss temperature dependence (Figure 29b), further suggesting the presence of paramagnetic defects in the O1a phase; the paramagnetic shift is negative due to the polarisation mechanism and becomes less negative with increasing temperature.

For this sample, the paramagnetic defects can only be observed in the ^{17}O NMR spectrum, because paramagnetic vanadium centres relax too quickly to be observed *via* ^{51}V NMR, and the hydrogen must be in a metallic environment, rather than being in the vicinity of a defect, because the ^{1}H NMR spectrum exhibits a Knight shift. Nevertheless, the paramagnetic centres dominate the bulk magnetic susceptibility measurements, rather than the metallic contribution; the greater density of paramagnetic defects in this sample also explains the higher Néel temperature observed in the bulk magnetic susceptibility (Figure 26).

18 ^{1}H NMR of Pristine VO_2 Thin Film

To determine whether the signal observed in the electrolyte gated VO_2 thin film was due to the gating process, the ^{1}H NMR was recorded for a 200 nm VO_2 thin film without electrolyte gating, again lightly hand grinding the film to pack it into the sample rotor. Figure 31 shows the conventional and T_1-filtered ^{1}H NMR spectra: unfortunately, there is a greater diamagnetic contamination of the pristine film which cannot be fully suppressed in the T_1-filtered spectrum and prevents direct comparison with the gated sample; however, no signal can be observed at 115 ppm in the T_1 filtered spectrum of the pristine VO_2, supporting the assertion that this signal in the gated VO_2 film is due to intercalated hydrogen in a metallic environment.

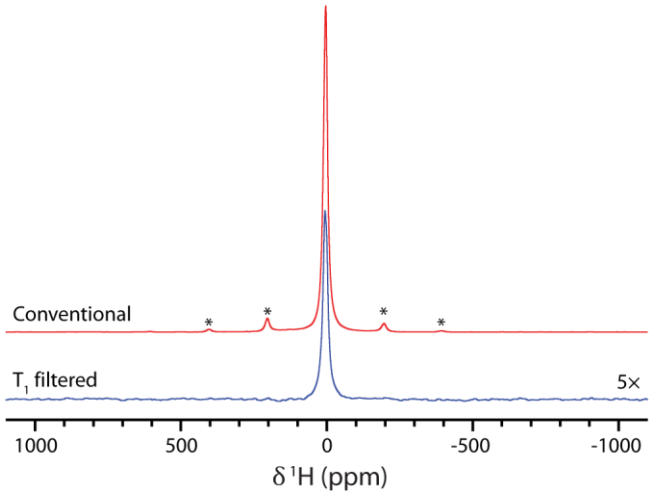

Figure 31: ^{1}H NMR spectra of a 200 nm VO_2 thin film on 0.5 mm TiO_2 without electrolyte gating, recorded at 4.70 T and 40 kHz MAS, with spinning sidebands marked with asterisks. The conventional spectrum was obtained with a recycle delay of 0.05 s using a DEPTH pulse sequence[20] and subtracting the background. The T_1-filtered spectrum was recorded by taking the

difference between background subtracted spectra with recycle delays of 0.05 s and 0.1 s, scaling the spectra so as to remove as much as possible the diamagnetic signals.

19 Deuteration of EMIm TFSI

Figure 32 shows the ^{1}H NMR spectrum of pristine EMIm TFSI and the ^{1}H and ^{2}H NMR spectra after stirring in D_2O, showing selective deuteration of the carbene hydrogen at 8.3 ppm.[21] Comparison of the integrations of the ^{1}H signals gives a deuteration of the carbene hydrogen of around 90 at%.

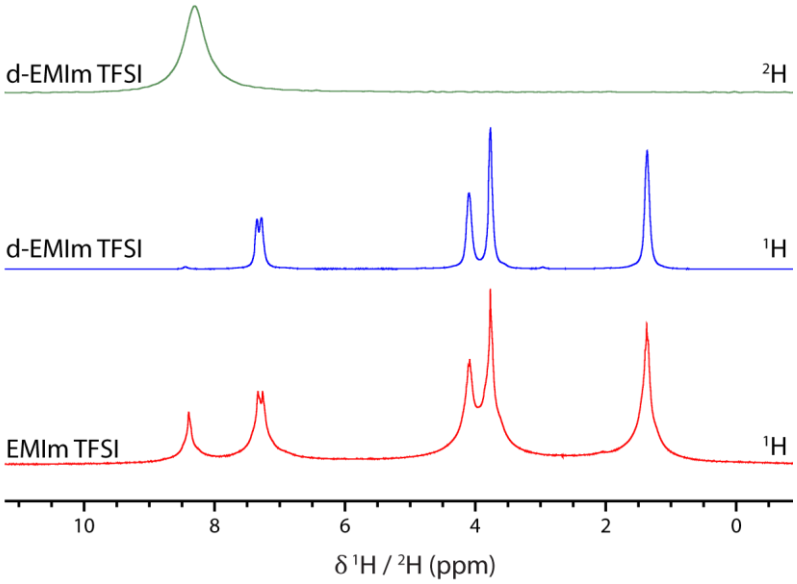

Figure 32: The ^{1}H NMR spectrum of pristine EMIm TFSI and the ^{1}H and ^{2}H NMR spectra after stirring in D_2O and subsequent drying, showing selective deuteration of the carbene hydrogen at 8.3 ppm. Spectra were recorded static at 7.05 T with a single-pulse experiment.

20 ^{2}H NMR of D_xVO_2 at Different Fields

Figure 33 shows the ^{2}H NMR spectra of VO_2 electrochemically hydrogenated at 100 °C with deuterated EMIm TFSI, recorded at different magnetic field strengths. At lower fields the sideband manifold is dominated by the axial quadrupolar tensor, indicative of an axial bonding environment, and at higher fields the sideband manifold is dominated by a shift anisotropy.

The spectra were also modelled at each field by combining the quadrupolar tensor with a chemical shift anisotropy (CSA) tensor, the parameters for which are shown in Table 5. These parameters were found by fitting the quadrupolar tensor at 4.70 T, the CSA tensor at 11.75 T and then the Euler angles (α, β, γ) relating these two tensors at 7.05 T, before iteratively minimising the difference at each field to yield a consistent fit. The solution is not perfect and may not be unique as changing the relative orientations of the tensors can lead to large and nonmonotonic changes in the sideband manifold, which are difficult to search using a local-optimisation routine. Nevertheless, the fit is reasonably consistent between fields and reproduces the major features, so the tensor parameters are likely to at least have the right order of magnitude.

The quadrupolar frequencies (ν_Q) of O1a and O1b were found to be ~270 kHz and ~230 kHz respectively; this suggests that the hydrogen bonding of the H/D atoms to other oxygen atoms in VO_2 is reasonably weak, as hydrogen bonding reduces the electric field gradient,[22,23] with slightly stronger hydrogen bonding in the O1b phase. Furthermore, as stronger hydrogen bonding would require a greater distortion to bring the oxygen atoms closer together, this means that a large distortion around the intercalated hydrogen atoms would not be expected in H_xVO_2.

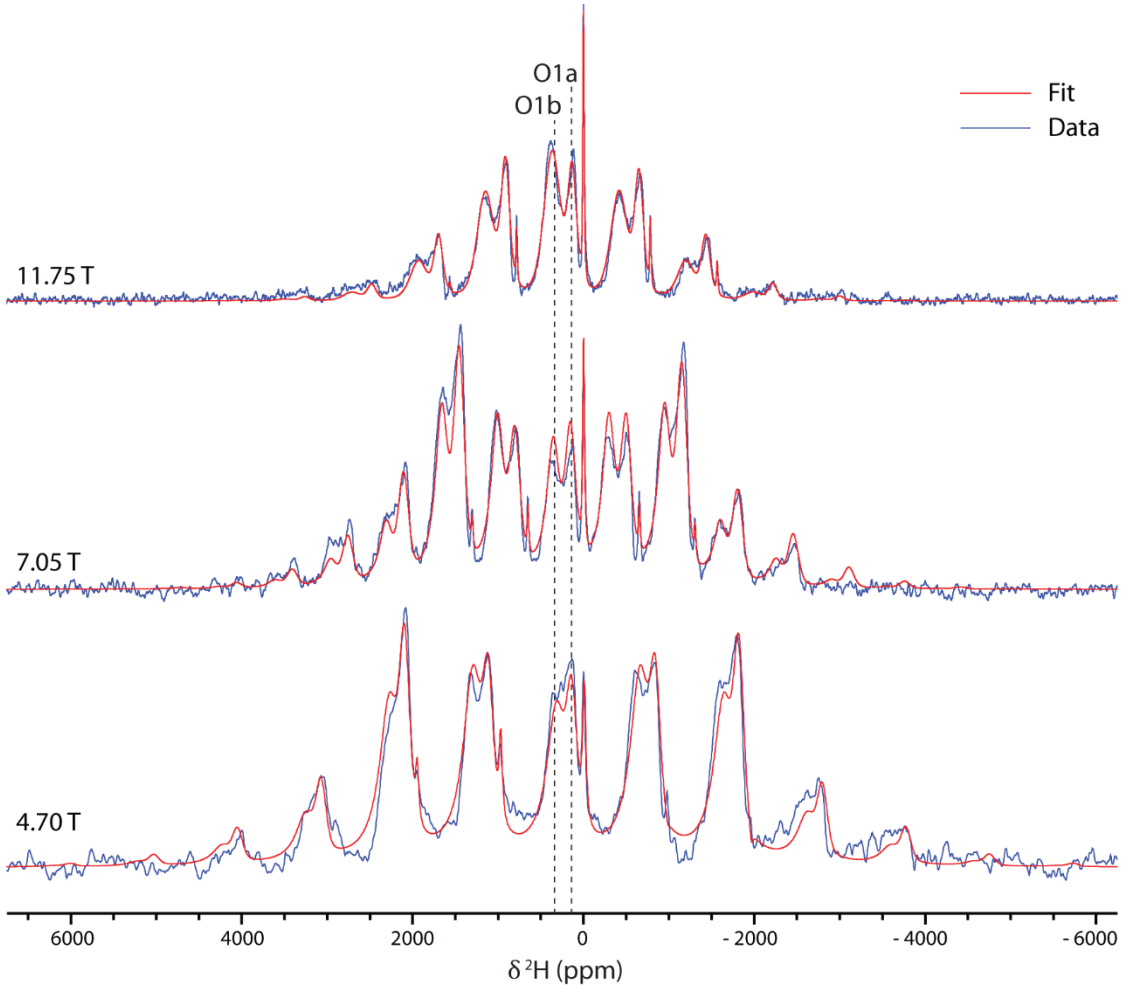

Figure 33: ^{2}H NMR spectra of VO_2 after electrochemical metallisation at 100 °C with deuterated EMIm TFSI, recorded at fields of 4.70 T, 7.05 T and 11.75 T using a Hahn echo pulse sequence. The spectra at 4.70 T and 7.05 T were recorded at 30 kHz MAS, the spectrum at 11.75 T was recorded at 60 kHz MAS.

Table 5: Fitted chemical shift anisotropy (CSA) and asymmetry (η), quadrupolar frequency (ν_Q) and asymmetry (η_Q), and Euler angles relating the two tensors (α, β, γ), for the deuterium environments in D_xVO_2.

	CSA /ppm	η	ν_Q /kHz	η_Q	α /°	β /°	γ /°
O1a	−1750	0.86	270	0.00	0	45	0
O1b	1410	0.99	230	0.00	0	45	0

21 Electrochemical Reduction with EIm TFSI and EM_2Im TFSI

Electrochemical metallisation experiments on VO_2 were also performed using different imidazolium-based ionic liquids: the more protic 1-ethylimidazolium bis(trifluoromethylsulfonyl)imide (EIm TFSI, Io-li-tec, 98%) and the less protic 1-ethyl-2,3-dimethylimidazolium bis(trifluoromethanesulfonyl)imide (EM_2Im TFSI, Tokyo Chemical Industry UK Ltd., 98%) (Figure 34). Similar degrees of hydrogenation were observed for all three ionic liquids (Table 6), however there is a difference in the voltage profiles observed during the electrochemical reduction (Figure 35): the acidity of the cations increases in the order EM_2Im < EMIm < EIm, and a less negative potential is observed following the same trend. At first glance the EM_2Im cation does not appear to have available protons, however it is possible to

deprotonate the methyl group to form an N-heterocylic olefin.[24] The differences observed in the degree of hydrogenation are ascribed to small differences between the energy of the hydrogenation reaction and the limiting side reaction(s).

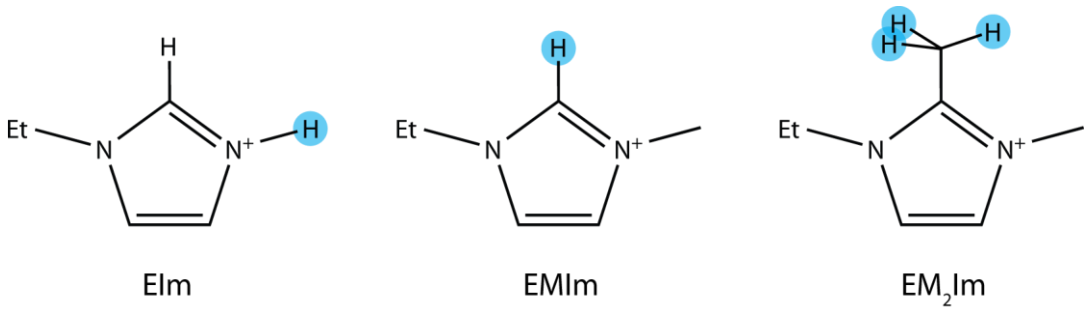

Figure 34: Different imidazolium-based ionic liquid cations, with the most acidic proton highlighted in each case.

Table 6: Degree of hydrogenation (x in H_xVO_2, quantitative ^1H NMR) and phases present (XRD) for VO_2 electrochemically metallised at room temperature with different ionic liquids.

	EIm	**EMIm**	**EM$_2$Im**
x	0.049(3)	0.037(2)	0.091(5)
Phases	M + O1a	M	M + O1a

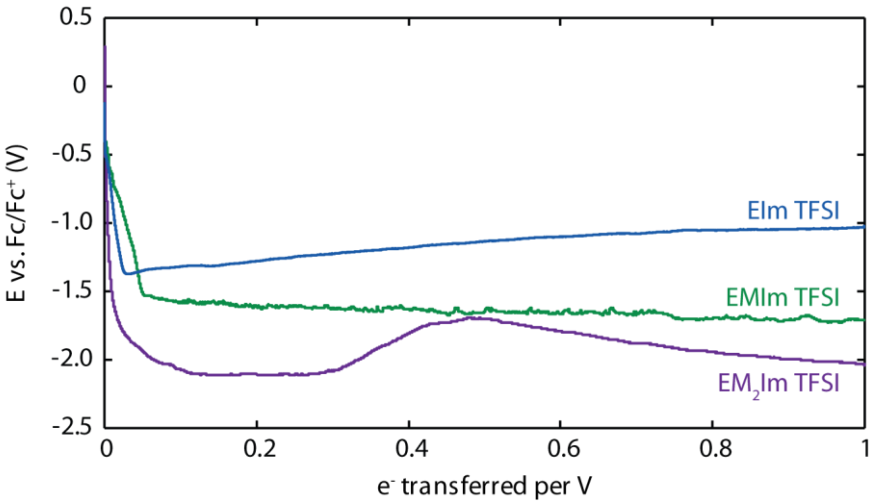

Figure 35: Voltage profiles for VO_2 electrochemically reduced at room temperature with different imidazolium-based ionic liquids.

22 Electrochemical Reduction with DEME TFSI

Another ionic liquid previously used in electrolyte gating experiments is diethylmethyl(2-methoxyethyl)ammonium bis(trifluoromethylsulfonyl)imide (DEME TFSI, cation shown in Figure 36a). Electrochemical reduction of bulk VO_2 with DEME TFSI also results in hydrogenation, as shown by ^1H NMR (Figure 36c). The DEME cation cannot form a stabilised N-heterocyclic carbene or olefin, as for imidazolium-based ionic liquids, so deprotonation must proceed by a different mechanism: one possibility is elimination of either the ethyl or methoxyethyl groups to form a neutral tertiary amine and ethene or methyl vinyl ether, respectively (Figure 36b, blue and green mechanisms); testing these mechanisms will be the subject of future work.

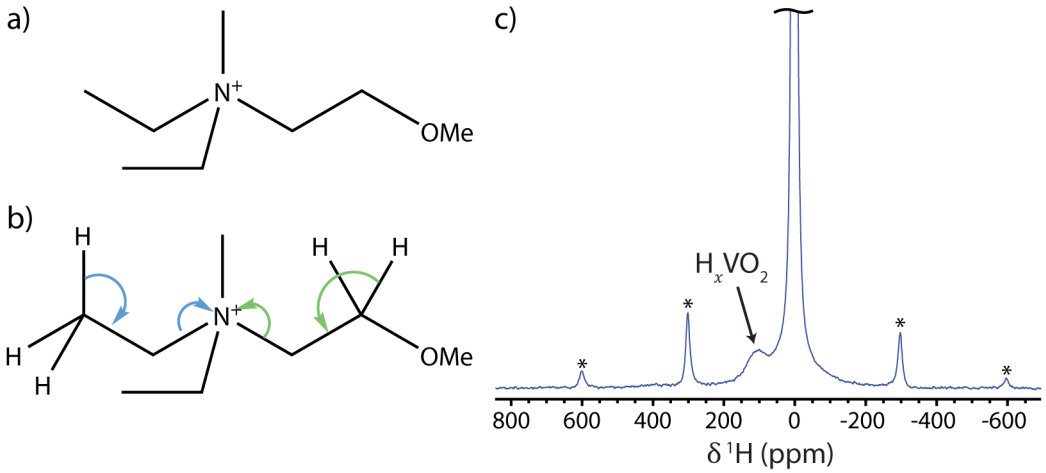

Figure 36: a) The DEME cation. b) Two possible elimination mechanisms for deprotonation (green and blue arrows respectively). c) ^{1}H NMR spectrum of VO_2 electrochemically reduced in DEME TFSI, recorded at 60 kHz MAS and 4.70 T with a Hahn echo pulse sequence. Sidebands are marked with asterisks.

23 Electrochemical Reduction as a Function of Potential

To determine the onset voltage of VO_2 hydrogenation, bulk VO_2 composite films were galvanostatically reduced using EMIm TFSI until the potential reached a specified voltage relative to the reference electrode, before being held at this voltage for 24 hours; Figure 37 shows the degree of hydrogenation determined by *ex-situ* quantitative ^{1}H NMR, as a function of this limiting voltage. There is not a sharp step in hydrogenation, but rather hydrogenation increases progressively with more negative voltage, which is consistent with a solid-solution rather than a two-phase reaction, before plateauing at ca. −0.75 V when some side-reaction prevents further hydrogenation. This is a less negative potential than in the galvanostatic experiment (ca. −1.6 V, see main text) because the overpotential is decreased when the potential is fixed and current allowed to respond, compared to when a fixed (higher) current is applied. The maximum amount of hydrogenation observed, x=0.021, is slightly lower than for galvanostatic reduction (x=0.037, see main text); this is ascribed to differences between batches of VO_2 composite films, most likely in particle size.

The onset voltage of VO_2 hydrogenation, ca. −0.5 V vs. Fc/Fc^{+}, is significantly less negative than the reported cathodic stability of EMIm TFSI (ca. −2.5 V vs. Fc/Fc^{+});[25] however, this is not surprising since electrolyte stability is highly dependent on the electrode against which it is measured. Although EMIm TFSI is stable down to a low voltage against an inert glassy carbon electrode, VO_2 catalyses the breakdown which can therefore happen at a much less negative voltage. This can clearly be seen in Figure 21a, when the current is reversed the cathodic limit on the Pt electrode is more than a volt more negative than it was on the VO_2 electrode. Furthermore, because the VO_2 partakes in the reaction, the change in free energy is not simply that required to decompose the electrolyte but is lowered by the free energy released by reducing the VO_2, and the voltage is thus correspondingly less negative.

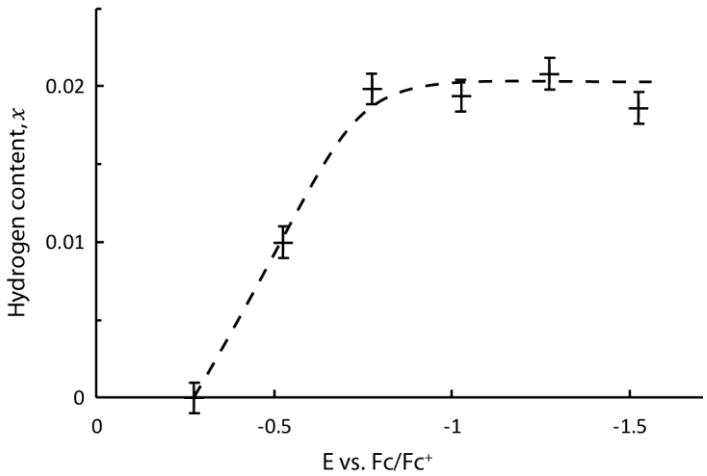

Figure 37: Hydrogen content x, from quantitative ^{1}H NMR, as a function of limiting voltage for electrochemical reduction of bulk VO_2 composite films with EMIm TFSI.

24 Variable Temperature XRD of M + O1a

To determine the effect of heating to above the MIT temperature on the two-phase M + O1a region of the phase diagram, variable temperature XRD patterns were recorded for VO_2 electrochemically metallised at 50 °C, $x \approx 0.1$. XRD patterns were recorded at room temperature, 100 °C, and then room temperature again, using a heated sample holder built in-house, in reflection mode, with a beryllium window. Figure 38 shows two expanded sections of the XRD patterns: in both room temperature patterns, there are two reflections around 2θ = 28° corresponding to the M and O1a phases, which coalesce into the single rutile reflection at 100 °C. The same effect is observed in the 2θ = 54° – 58° region, and in particular the orthorhombic peak at 2θ = 54.7° is not present in the 100 °C pattern. This shows that the two-phase M + O1a region of the phase diagram at room temperature becomes a single rutile (R) phase above the MIT, due to a greater solubility of hydrogen in the rutile phase compared to the monoclinic phase. The M and O1a phases are again observed after cooling down to room temperature, indicating that this phase transition is reversible.

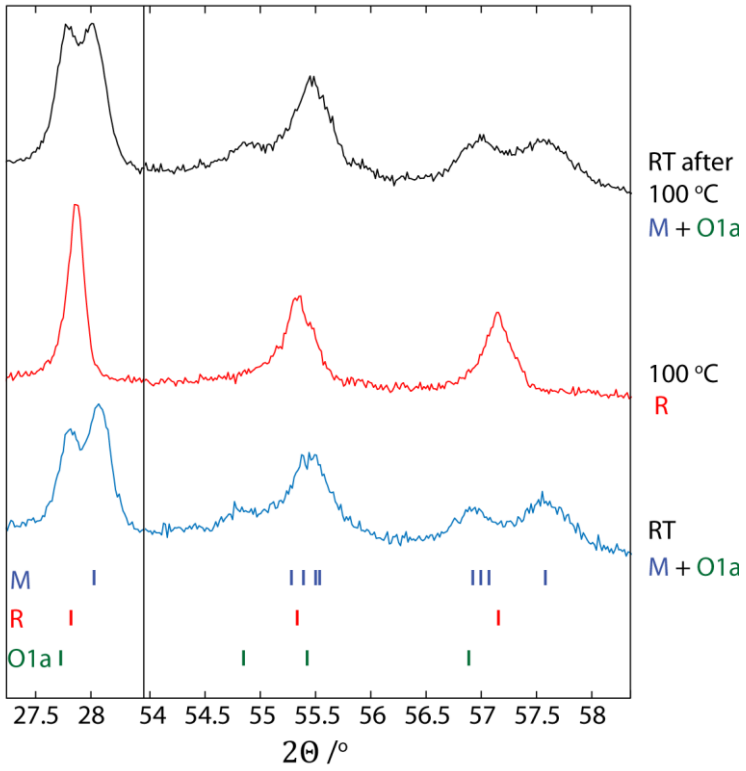

Figure 38: Selected regions of the XRD patterns of VO_2 electrochemically metallised at 50 °C, recorded at room temperature, 100 °C, and then room temperature again.

25 References

(1) De Souza, A. C.; Pires, A. T. N.; Soldi, V. Thermal Stability of Ferrocene Derivatives and Ferrocene-Containing Polyamides. *J. Therm. Anal. Calorim.* **2002**, *70* (2), 405–414.

(2) Liebsch, A.; Ishida, H.; Bihlmayer, G. Coulomb Correlations and Orbital Polarization in the Metal-Insulator Transition of VO2. *Phys. Rev. B* **2005**, *71* (8), 085109.

(3) Eyert, V. VO2: A Novel View from Band Theory. *Phys. Rev. Lett.* **2011**, *107* (1), 2–5.

(4) Brito, W. H.; Aguiar, M. C. O.; Haule, K.; Kotliar, G. Metal-Insulator Transition in VO2: A DFT + DMFT Perspective. *Phys. Rev. Lett.* **2016**, *117* (5), 056402.

(5) Clark, S. J.; Segall, M. D.; Pickard, C. J.; Hasnip, P. J.; Probert, M. J.; Refson, K.; Payne, M. C. First Principles Methods Using {CASTEP}. *Z. Krist.* **2005**, *220*, 567–570.

(6) Pickard, C. J.; Mauri, F. All-Electron Magnetic Response with Pseudopotentials: {NMR} Chemical Shifts. *Phys. Rev. B* **2001**, *63*, 245101.

(7) Yates, J. R.; Pickard, C. J.; Mauri, F. Calculation of NMR Chemical Shifts for Extended Systems Using Ultrasoft Pseudopotentials. *Phys. Rev. B* **2007**, *76*, 24401.

(8) Profeta, M.; Mauri, F.; Pickard, C. J. Accurate First Principles Prediction of 17 O NMR Parameters in SiO 2 : Assignment of the Zeolite Ferrierite Spectrum. *J. Am. Chem. Soc.* **2003**, *125* (2), 541–548.

(9) Perdew, J. P.; Burke, K.; Ernzerhof, M. Generalized Gradient Approximation Made Simple. *Phys. Rev. Lett.* **1996**, *77* (18), 3865–3868.

(10) MacKenzie, K. J.; Smith, M. E. *Multinuclear Solid-State Nuclear Magnetic Resonance of Inorganic Materials*; 2002.

(11) Geller, S.; Romo, P.; Remeika, J. P. Refinement of the Structure of Scandium Sesquioxide. *Zeitschrift für Krist. Mater.* **1967**, *124* (1–6), 136–142.

(12) Restori, R.; Schwarzenbach, D.; Schneider, J. R. Charge Density in Rutile, TiO2. *Acta Crystallogr. Sect. B Struct. Sci.* **1987**, *43* (3), 251–257.

(13) Bachmann, H.G.; Ahmed, F.R.; Barnes, W. H. The Crystal Structure of Vanadium Pentoxide. *Zeitschrift fuer Krist. Krist. Krist. Krist.* **1961**, *115*, 110–131.

(14) Longo, J. M.; P, K. A Refinement of the Structure of VO2. *Acta Chem. Scand.* **1970**, *24* (2), 420.

(15) Bonhomme, C.; Gervais, C.; Babonneau Florenceand Coelho, C.; Pourpoint, F.; Azais, T.; Ashbrook, S. E.; Griffin, J. M.; Yates, J. R.; Mauri, F.; Pickard, C. J. First-Principles Calculation of NMR Parameters Using the Gauge Including Projector Augmented Wave Method: A Chemist's Point of View. *Chem. Rev.* **2012**, *112*, 5733.

(16) Chippindale, A. M.; Dickens, P. G.; Powell, A. V. Synthesis, Characterization, and Inelastic Neutron Scattering Study of Hydrogen Insertion Compounds of VO2(Rutile). *J. Solid State Chem.* **1991**, *93* (2), 526–533.

(17) Thurber, K. R.; Tycko, R. Measurement of Sample Temperatures under Magic-Angle Spinning from the Chemical Shift and Spin-Lattice Relaxation Rate of 79Br in KBr Powder. *J. Magn. Reson.* **2009**, *196* (1), 84–87.

(18) Mydosh, J. A. *Spin Glasses: An Experimental Introduction*; Taylor & Francis: London, 1993.

(19) Carlier, D.; Ménétrier, M.; Grey, C. P.; Delmas, C.; Ceder, G. Understanding the NMR Shifts in Paramagnetic Transition Metal Oxides Using Density Functional Theory Calculations. *Phys. Rev. B* **2003**, *67* (17), 174103.

(20) Robin Bendall, M.; Gordon, R. E. Depth and Refocusing Pulses Designed for Multipulse NMR with Surface Coils. *J. Magn. Reson.* **1983**, *53* (3), 365–385.

(21) Fujii, K.; Soejima, Y.; Kyoshoin, Y.; Fukuda, S.; Kanzaki, R.; Umebayashi, Y.; Yamaguchi, T.; Ishiguro, S.; Takamuku, T. Liquid Structure of Room-Temperature Ionic Liquid, 1-Ethyl-3-Methylimidazolium Bis-(Trifluoromethanesulfonyl) Imide. *J. Phys. Chem. B* **2008**, *112* (14), 4329–4336.

(22) Kim, G.; Blanc, F.; Hu, Y. Y.; Grey, C. P. Understanding the Conduction Mechanism of the Protonic Conductor CsH2PO4 by Solid-State NMR Spectroscopy. *J. Phys. Chem. C* **2013**, *117* (13), 6504–6515.

(23) Blinc, R.; Hadži, D. Deuteron Quadrupole Coupling and Hydrogen Bonding in Crystals. *Nature* **1966**, *212* (5068), 1307–1309.

(24) Saptal, V. B.; Bhanage, B. M. N-Heterocyclic Olefins as Robust Organocatalyst for the Chemical Conversion of Carbon Dioxide to Value-Added Chemicals. *ChemSusChem* **2016**, *9* (15), 1980–1985.

(25) Mousavi, M. P. S.; Dittmer, A. J.; Wilson, B. E.; Hu, J.; Stein, A.; Bühlmann, P. Unbiased Quantification of the Electrochemical Stability Limits of Electrolytes and Ionic Liquids. *J. Electrochem. Soc.* **2015**, *162* (12), A2250–A2258.